

AperTO - Archivio Istituzionale Open Access dell'Università di Torino

Dissolving dolomite in a stable UHP mineral assemblage: evidence from Cal-Dol marbles of the Dora-Maira Massif (Italian Western Alps).

This is the author's manuscript

Original Citation:

Availability:

This version is available <http://hdl.handle.net/2318/1614587> since 2017-05-17T09:48:19Z

Published version:

DOI:10.2138/am-2017-5761

Terms of use:

Open Access

Anyone can freely access the full text of works made available as "Open Access". Works made available under a Creative Commons license can be used according to the terms and conditions of said license. Use of all other works requires consent of the right holder (author or publisher) if not exempted from copyright protection by the applicable law.

(Article begins on next page)

Revision 1

Dissolving dolomite in a stable UHP mineral assemblage: evidence from Cal-Dol marbles of the Dora-Maira Massif (Italian Western Alps)

SIMONA FERRANDO¹, CHIARA GROPPPO^{1,2}, MARIA LUCE FREZZOTTI³, DANIELE CASTELLI¹,
ALEXANDER PROYER⁴

¹ Department of Earth Sciences, University of Torino, Via Valperga Caluso 35, I-10125 Torino,
Italy

² IGG-CNR, Via Valperga Caluso 35, I-10125 Torino, Italy

³ Department of Earth and Environmental Sciences, University of Milano Bicocca, Piazza della
Scienza 4, I-20126 Milano, Italy

⁴ Department of Geology, University of Botswana, Private Bag UB 00704, Gaborone, Botswana

ABSTRACT

In deep and cold subduction such as that experienced by the UHP Units of the Western Alps, carbon dissolution is a relevant mechanism for carbon transfer from the slab into the mantle. The UHP impure Cal-Dol-marbles from the Dora-Maira Massif are studied to investigate the poorly known evolution of dolomite during deep subduction. Dolomite shows four stages of growth, from pre-Alpine to early-retrograde Alpine, coupled with chemical variations and distinct included mineral assemblages. To explain the evidence for growth and partial reabsorption of dolomite through HP prograde, UHP peak, and UHP early-retrograde Alpine metamorphism, a chemically simple marble (Cal, Dol, Di, Fo, and retrograde Atg, Tr, Mg-Chl) has been studied in detail.

25 Microstructural relationships, coupled with mineral chemistry, indicate the growth of the
26 assemblage dolomite+diopside+forsterite±aragonite during *HP* prograde, *UHP* peak, and *UHP*
27 early-retrograde evolution.

28 Mixed-volatile *P-T* projection modelled in the simple CaO-(FeO)-MgO-SiO₂-H₂O-CO₂ system and
29 *T/P-X(CO₂)* petrogenetic grids and pseudosections predict the prograde (1.7 GPa, 560°C) growth of
30 dolomite in equilibrium with diopside and forsterite through the breakdown of antigorite +
31 aragonite. In a H₂O-CO₂ saturated system, the subsequent *HP-UHP* evolution is predicted in the
32 Di+Fo+Dol+Arg stability field in equilibrium with a dominantly aqueous COH fluid
33 (0.0003<*X(CO₂)*<0.0008), whose composition is internally buffered by the equilibrium assemblage.
34 Thermodynamic modelling indicates that neither the consumption nor the growth of new dolomite
35 generations at *UHP* conditions can have been induced by metamorphic reactions. The abundant
36 primary H₂O + Cal + Dol + Cl-rich Tr + Cl-rich Tlc ± chloride fluid inclusions present in *UHP* Cpx
37 indicate that a dominantly aqueous, saline (salinity > 26.3 wt% of NaCl_{eq}) COH fluid, containing
38 Ca, Mg, and Si as dissolved cations was present during the growth of the *UHP* assemblage
39 Dol+Cpx+Ol+Arg.

40 The complex zoning of dolomite is therefore interpreted as due to protracted episodes of dissolution
41 and precipitation in saline aqueous fluids at *HP/UHP* conditions. Kinetics of dolomite dissolution in
42 aqueous fluids is poorly known, and experimental and thermodynamic data under *HP* conditions are
43 still lacking. Data on calcite indicate that dissolution at *HP* is enhanced by a prograde increase in
44 both *P* and *T*, by high salinity in aqueous fluids, and/or low pH conditions. In the studied marble,
45 the *P-T* path and the occurrence of free high-saline fluids represent favourable conditions i) for the
46 inferred dissolution-precipitation processes of the stable dolomite in a closed system; ii) for possible
47 migration of the dissolved carbonate, if the system would have been open during subduction.

48

49 **Keywords:** subduction, zoned dolomite, cathodoluminescence, micro-Raman spectroscopy,
50 thermodynamic modelling, COH fluid, dissolution-precipitation.

51

52

INTRODUCTION

53 In the long-term global carbon cycle, the flux of carbon released in the Earth's interior by
54 subduction is directly connected with that released from volcanic arcs and, ultimately, can
55 contribute to climate variability. The still poorly constrained nature and composition of the COH
56 fluids generated during deep (i.e., at ultra-high pressure conditions) subduction, such as their fate in
57 the Earth's interior, are responsible for the highly controversial estimations of carbon fluxes to the
58 exosphere (e.g., Kelemen and Manning, 2015). In this context, metamorphic evolution of
59 carbonates during subduction plays an important role, because they are relevant constituents of the
60 altered oceanic crust and of the sedimentary materials in convergent settings.

61 Thermodynamic modelling on natural samples and experimental data indicate that carbonates are
62 resistant to metamorphic decarbonation and to melting during relatively cold subduction, i.e. such
63 as that experienced by the Units of the Western Alps (e.g. Castelli, 1991; Ballèvre and Lagabrielle,
64 1994; Molina and Poli, 2000; Kerrick and Connolly, 2001 a, b; Connolly, 2005; Dasgupta et al.,
65 2005; Gorman et al., 2006; Castelli et al., 2007; Poli et al., 2009; Mposkos et al., 2010), although
66 some exceptions from natural samples are reported (e.g., Cook-Kollars et al., 2014). Experiments
67 on (Ca, Fe, Mg)-carbonates indicate that they are stable at high pressure (e.g., Gorman et al., 2006;
68 Poli et al., 2009; Dasgupta and Hirschmann, 2010; Tumiati et al., 2013; Schmidt and Poli, 2014).
69 Experiments on a basaltic composition in the presence of a H₂O-CO₂ mixed fluid demonstrate that
70 calcite is stable at $P \leq 1.4$ GPa, dolomite at P between 1.4 and 1.8 GPa, and dolomite and magnesite
71 at $P \geq 1.8$ GPa (Molina and Poli, 2000). Experiments at high pressure show that dolomite can be
72 stable up to ca. 5 GPa and 600°C (e.g., Buob et al., 2006; Hammouda et al., 2011; Luth, 2001;
73 Martinez et al., 1996; Morlidge et al., 2006; Sato and Katsura, 2001). At higher P - T conditions,
74 dolomite breakdowns to produce magnesite + aragonite, and the natural occurrence of this mineral
75 assemblage has been considered as evidence for geothermic gradients near or below the “forbidden
76 zone” (i.e. $< 5^\circ\text{C}/\text{km}$; e.g. Zhu and Ogasawara, 2002; Zhang et al., 2003; Proyer et al., 2013).

77 However equilibrium/disequilibrium microstructures between magnesite and aragonite and their Fe-
78 contents must be carefully considered (e.g., Smit et al., 2008; Korsakov et al., 2009; Proyer et al.,
79 2013; Li et al., 2014; Liu et al., 2015).

80 Although thermodynamic modelling and experimental studies suggest that carbonates are mostly
81 recycled into the mantle at subduction zones, increasing natural evidence testifies for a significant
82 mobility of COH fluids during subduction. During the prograde evolution or at peak *P-T* conditions,
83 fluid-rock interactions between COH fluids and surrounding rocks can occur either at a local-scale,
84 i.e. in a relatively closed system (e.g. Philippot and Selverstone 1991; Ishida et al., 2003; Frezzotti
85 et al., 2011; Gao et al., 2014), or in an open system, as testified by the occurrence of veins and
86 alteration zones within eclogite-facies rocks (e.g., Gao and Klemd, 2001; Ague and Nicolescu,
87 2014). Moreover, the wide occurrence of COH fluids during deep subduction is suggested by the
88 relatively common presence of carbonates, often associated with microdiamonds, as solids
89 precipitated in fluid inclusions and multiphase-solid inclusions in high pressure (*HP*) and ultra-high
90 pressure (*UHP*) crustal and mantle rocks from Dabie-Sulu (e.g., Fu et al., 2003; Ferrando et al.,
91 2005; Gao et al., 2014), Kokchetav (e.g., Dobrzhinetskaya et al., 2003; Hwang et al., 2006;
92 Korsakov and Hermann, 2006), Western Gneiss Region (e.g., Svensen et al., 1999; Carswell and
93 van Roermund, 2005), Moldanubian Zone (Naemura et al., 2009), Erzgebirge (e.g.,
94 Dobrzhinetskaya et al., 2007), Rhodope (Mposkos et al., 2009), Tauern Window (Selverstone et al.,
95 1992), Dora-Maira (e.g., Philippot et al., 1995; Ferrando et al., 2009), Monviso (Philippot and
96 Selverstone, 1991), Lago di Cignana (Frezzotti et al., 2011; for a review see Frezzotti and Ferrando,
97 2015). Whereas in deep and hot subduction regimes, such as that recorded by the Kokchetav
98 Massif, the possible melting of carbonates can generate carbonatitic liquids rich in CO₂ (e.g.,
99 Korsakov and Hermann, 2006; Grassi and Schmidt, 2011; Gao et al., 2014; Poli, 2015), in deep and
100 cold subduction settings, such as the *UHP* Units of the Western Alps, the carbon fractionation in a
101 liquid phase can be induced by dissolution of carbonates in aqueous fluids released by the
102 breakdown of hydrous phases (e.g., Caciagli and Manning, 2003; Frezzotti et al., 2011, 2014;

103 Manning et al., 2013; Pan et al., 2013). Thermodynamic modelling in H₂O-CO₂ mixed volatile
104 systems indicates that these fluids are H₂O-dominated (e.g., Castelli, 1991; Wang and Liou, 1993;
105 Ballèvre and Lagabriele, 1994; Kato et al., 1997; Ogasawara et al., 1998; Omori et al., 1998;
106 Ogasawara and Aoki, 2005; Castelli et al., 2007; Proyer et al., 2008; Massonne, 2011; Droop, 2013;
107 Liu et al., 2015). Accordingly, Raman analyses of C species in UHP aqueous fluid inclusions in
108 oceanic metasediments from Lago di Cignana (Frezzotti et al., 2011; 2014) revealed the presence of
109 oxidized carbon dissolved as CO₃²⁻(aq) and HCO₃⁻(aq), along with hydrous and hydrated
110 carbonates and diamond, and no detectable CO₂. Recent experimental and theoretical researches on
111 dissolution of carbonates are in agreement with observations on natural samples (Manning et al.,
112 2013 and references therein). The spectroscopy experiments at 25-650 °C and 0.5-30 GPa
113 performed by Martinez et al. (2004), Sanchez-Valle et al. (2013) and Facq et al. (2014) reveal the
114 dominant presence of carbonate ions, similar to those found in the Lago di Cignana rocks, in UHP
115 aqueous fluids.

116 Among carbonates, dolomite from UHP rocks is the best candidate to investigate the poorly known
117 evolution of carbonates during cold subduction. In fact, experiments on dolomite, calcite and
118 magnesite at 700-800°C and 0.3 GPa (Davis et al., 2011) reveal that the constant rate of grain
119 growth for dolomite is three orders of magnitude lower than that of calcite and more than one order
120 lower than that of magnesite. This implies that zoning is a common feature in dolomite, making it
121 able to preserve evidence for its prograde-to-peak evolution (e.g., Li et al., 2014). Moreover, the
122 process of dolomite dissolution still remains unclear in both sedimentary and metamorphic
123 petrology. In fact, the thermodynamics of dolomite solubility in water are difficult to be
124 constrained, even at diagenetic conditions, because of its slow rate of dissolution and its
125 incongruent dissolution behaviour (e.g., Busenberg and Plummer, 1982; Hardie, 1987).

126 Polymetamorphic impure calcite-dolomite marbles from the well known UHP Brossasco-Isasca
127 Unit of the southern Dora-Maira Massif (Italian western Alps) (Fig. 1) are promising rocks to
128 investigate the HP-UHP dolomite evolution. In this paper, we describe zoned dolomite

129 porphyroclasts showing evidence for their destabilization and growth close to metamorphic peak *P*-
130 *T* conditions, and occurring in impure calcite-dolomite marbles belonging to different chemical
131 systems. To characterize the processes involved in the consumption/growth of dolomite, a detailed
132 microstructural study, coupled with mineral chemistry, thermodynamic modeling and fluid
133 inclusion study are performed on a sample referring to the simple CaO-(FeO)-MgO-SiO₂-COH
134 system. The data suggest dissolution-precipitation mechanisms, instead of metamorphic reactions,
135 to explain the dolomite evolution. To our knowledge, this is the first report of dolomite dissolution-
136 precipitation processes occurred in marbles from continental crust involved in cold subduction. Our
137 results suggest that in cold subduction settings, carbonate dissolution in aqueous fluids, rather than
138 metamorphic decarbonation, is the crucial process controlling the mobility of carbon in and from
139 the subducting plate.

140

141 **GEOLOGICAL BACKGROUND AND FIELD DESCRIPTION**

142 The Brossasco-Isasca Unit (BIU) is a small tectonic sheet of continental crust belonging to the
143 Southern Dora-Maira Massif (Compagnoni et al., 2012; Fig. 1a). Two lithostratigraphic complexes
144 have been distinguished in the BIU (Compagnoni et al., 1995). The “Monometamorphic Complex”
145 is derived from the Alpine tectonic and metamorphic reworking of Permian (275 Ma; Gebauer et
146 al., 1997) granitoids and consists of metagranitoid, augen-gneiss, fine-grained orthogneiss, garnet +
147 jadeite + kyanite + quartz granofels, and the Mg-metasomatic rocks (pyrope-bearing whiteschist) in
148 which natural coesite was discovered and studied for the first time (Chopin, 1984). The
149 “Polymetamorphic Complex” is derived from the Alpine reworking of a Variscan amphibolite-
150 facies metamorphic basement that locally experienced a low-*P* static recrystallisation related to the
151 intrusion of the Permian granitoids (Fig. 1b; Groppo et al., 2007a). This Complex mainly consists of
152 paraschists that include bodies of eclogites, marbles, and calc-silicate rocks.

153 The *P-T-t* Alpine evolution of the BIU has been constrained from different lithologies such as
154 whiteschist (Duchêne et al., 1997; Gebauer et al., 1997; Compagnoni and Hirajima, 2001; Hermann,

155 2003; Vaggelli et al., 2006; Ferrando et al., 2009; Gauthiez-Putallaz et al., 2016), marble (Ferraris et
156 al., 2005; Di Vincenzo et al., 2006; Castelli et al. 2007; Groppo et al., 2007a), eclogite (Di
157 Vincenzo et al., 2006; Groppo et al., 2007b), calc-silicate rocks (Rubatto and Hermann, 2001), and
158 orthogneiss (Di Vincenzo et al., 2006). Figure 1b reports the Variscan and Alpine evolution of the
159 BIU as inferred from all these data. The Alpine BIU evolution is characterized by: 1) a prograde
160 stage at ~1.6 GPa and ≤ 600 °C, recorded in relict metapelitic xenoliths partly metasomatized during
161 stage 2; 2) prograde dehydration reactions and local Mg-metasomatism along shear zones (i.e.,
162 subduction-related whiteschist genesis) at 1.7–2.1 GPa and 560–590 °C; 3) prograde dehydration
163 reactions, and local progressive Mg-metasomatism, with development of a (relict) prograde
164 foliation recorded in whiteschists and marbles, in the large *P-T* range of ~2.2-2.8 GPa and ~590-640
165 °C (i.e., up to the quartz-coesite transition) and dated at ~41-35 Ma; 4) local UHP prograde
166 dehydration reactions in whiteschists at 3.5-4.0 GPa and 700-730°C dated at ~ 35 Ma, and UHP
167 peak recorded by all studied lithologies at ~4.0–4.5 GPa and 730-750 °C and dated at ~35 Ma; 5) an
168 early, almost isothermal, decompression with development of the UHP main regional foliation,
169 locally observed in the BIU lithologies, at ~3.7-4.0 GPa and ~720-740°C; 6) a decompression
170 coupled with cooling recorded in marbles and whiteschists at ~3.0 GPa and ~700°C (i.e., still in the
171 coesite stability field); 7) a decompression coupled with cooling recorded in marbles, eclogites and
172 whiteschists at ~2.5-2.7 GPa and ~650-690°C (i.e., in the quartz stability field); 8) an almost
173 isothermal decompression recorded in marbles at ~2.0 GPa and ~640-660°C; 9) a further
174 decompression with moderate cooling recorded in marbles, eclogites, whiteschists and
175 orthogneisses at ~1.2-1.4 GPa and ~610-640°C; 10) a decompression coupled with cooling recorded
176 in calc-silicate rocks and marbles at ~0.7-1.0 GPa and ~530°C and dated at ~33 Ma; 11) a
177 decompression coupled with heating recorded in calc-silicate rocks and marbles at ~0.5 GPa and
178 ~550°C and dated at ~32 Ma, and a further cooling at greenschist facies conditions.

179 In the BIU, pure and impure calcite marbles, impure calcite-dolomite marbles, and carbonate-
180 silicate rocks are usually hosted within the paraschists of the “Polymetamorphic Complex” as
181 lenses, from a few metres to tens of metres long and from a few dm to several metres thick, that
182 locally contain thin discontinuous interlayers of micaschist and boudins of eclogite. The
183 polymetamorphic evolution of these marbles is usually described by variations in the silicate
184 mineral assemblages. Pre-Alpine minerals are mainly observed in calcite-dolomite marbles and
185 consist of HT minerals such as spinel and ilmenite (Groppo et al., 2007a). Prograde phengite has
186 been recognised in calcite marbles (Ferraris et al., 2005). UHP Na-clinopyroxene, garnet (or epidote
187 *s.l.*), phengite, and rutile (or titanite) are observed in calcite marbles (Ferraris et al., 2005; Castelli et
188 al., 2007) and in calc-silicate rocks (Rubatto and Hermann, 2001), whereas UHP corundum and
189 chlorite locally occur in calcite-dolomite marbles (Castelli et al., 2007). Retrograde garnet, epidote
190 *s.l.*, white mica, Mg-hornblende, diopside + plagioclase symplectites, biotite, titanite, quartz are
191 recognised in calcite marbles (Ferraris et al., 2005; Castelli et al., 2007) and in calc-silicate rocks
192 (Rubatto and Hermann, 2001), and chlorite, Na-margarite, högbomite, and ilmenite in calcite-
193 dolomite marbles (Castelli et al., 2007; Groppo et al., 2007a).

194 The studied samples have been collected from the largest marble lenses in the BIU, i.e. those of
195 Costa Monforte (Castelli et al., 2007) and Isasca (Fig. 1a), both characterized by a medium- to
196 coarse-grained fabric with local occurrence of mylonitic fabric within shear zones. These lenses
197 consists of impure calcite-dolomite marbles with scattered and lens-shaped silicates-rich domains,
198 from few centimetres to some decimetres in thickness (i.e., banded marbles), set parallel to the
199 early-retrograde UHP regional foliation (Fig. 1b) and characterized by distinct mineral
200 assemblages. The banded structure likely derives from primary differences in the marble’s protolith.
201 Most of the impure calcite-dolomite marbles can be described in the complex Na₂O-K₂O-CaO-FeO-
202 MgO-Al₂O₃-SiO₂-COH (NKCFMAS-COH) system (i.e., white mica ± Cpx ± Zo ± Grt ± Amp ±
203 Chl ± Qz calcite-dolomite marbles; mineral abbreviation according to Whitney and Evans, 2010) or
204 in the (Na₂O)-CaO-FeO-MgO-(Al₂O₃)-SiO₂-COH ((N)CFM(A)S-COH) system (i.e., Cpx ± Amp ±

205 Chl calcite-dolomite marbles). On the contrary, Chl ± Atg ± Tr ± Ol ± Di calcite-dolomite marbles
206 referring to the CaO-(FeO)-MgO-SiO₂-COH (C(F)MS-COH) system only occur in minor volumes
207 (Table 1). Evidence for chemical interaction among the chemically distinct layers are lacking.

208

209

METHODS

210

211 The characterization of mineral assemblages, microstructures, mineral phase compositions and fluid
212 inclusions have been obtained combining optical, cathodoluminescence and back-scattered electron
213 microscope observations, WDS and SEM-EDS analyses, micro-Raman spectroscopy and micro-
214 XRF maps.

215

Cathodoluminescence

217 Cathodoluminescence images were collected at the Department of Earth Sciences (University of
218 Torino, Italy) with a microscope performed with CITL 8200 mk3 equipment. Operating conditions
219 were 17 kV and 400 mA. The luminescence of minerals, in particular of carbonates (e.g.,
220 Habermann et al., 1996, 1998), is suppressed by some major or trace elements (typically Fe, Sr) and
221 activated by others (typically Mn, Na, Ti, Sm, Dy, Tb). The Fe/Mn ratio, in particular, is more
222 important than their absolute concentrations (e.g., Jarc and Zupancic, 2009). Crystallographic
223 structure, reticular defects, and crystallographic orientation of minerals also influence their
224 luminescence (e.g., Schertl et al., 2004).

225

Mineral chemistry

227 Compositions of minerals in sample DM675 were obtained using a JEOL 8200 Superprobe (WDS)
228 at the Department of Earth Sciences, University of Milano (Italy). Acceleration voltage was set to
229 15 kV, beam current was 5 nA, beam diameter was 5 µm. Back-scattered electron images and
230 composition of minerals from the other samples were collected with a JEOL JSM 6310 scanning

231 electron microscope equipped with an Oxford Link ISIS EDS spectrometer and a Microspec WDS
232 spectrometer (for Na and F) at the University of Graz (Austria). Analytical conditions were 15 kV
233 accelerating voltage and 6 nA probe current for silicates and 2 nA for carbonates, respectively, with
234 a 1–2 μm diameter of the focused beam. In both cases, natural minerals were used as standards and
235 a $\rho\Phi Z$ routine was used for matrix correction. Mineral phase compositions are reported in Tables 2,
236 3 and Supplementary Table S1.

237 The solids within primary fluid inclusions in diopside (sample DM675) were analyzed with a
238 Cambridge Stereoscan 360 SEM equipped with an EDS Energy 200 and a Pentafet detector (Oxford
239 Instruments) at the Department of Earth Sciences, University of Torino. The operating conditions
240 were as follows: 50 s counting time and 15 kV accelerating voltage. SEM–EDS qualitative data
241 (spot size = 2 μm) were acquired and processed using the Microanalysis Suite Issue 12, INCA Suite
242 version 4.01.

243

244 **Micro-Raman spectroscopy**

245 Micro-Raman spectra and maps were acquired using the integrated micro/macro-Raman LABRAM
246 HRVIS (Horiba Jobin Yvon Instruments) of the Interdepartmental Center “G. Scansetti”
247 (Department of Earth Sciences, University of Torino, Italy), equipped with a computer-controlled,
248 automated X–Y mapping stage. Excitation lines at 532 nm (solid-state Nd laser and 80 mW of
249 emission power) were used, with Edge filter and a grating of 600 grooves/mm. Calibration was
250 performed using the 520.6 cm^{-1} Si band. Each spectrum was collected by 3–5 accumulations of 5–20
251 s and with a laser spot of 2 μm . The map of 16 μm x 16 μm , with steps of 0.5 μm and a laser spot of
252 2x2 μm , was acquired by one accumulation of 5 s, each step.

253

254 **Micro-X-ray fluorescence (μ -XRF) map**

255 The micro-XRF map of the whole thin section of sample DM675 were acquired using a μ -XRF
256 Eagle III-XPL spectrometer equipped with an EDS Si(Li) detector and with an Edax Vision32

257 microanalytical system (Department of Earth Sciences, University of Torino, Italy). The operating
258 conditions were as follows: 100 ms counting time, 40 kV accelerating voltage and a probe current
259 of 900 μ A. A spatial resolution of about 65 μ m in both x and y directions was used. Quantitative
260 modal percentages of each mineral were obtained by processing the μ -XRF maps with the software
261 program “Petromod” (Cossio et al. 2002).

262

263 **Phase diagrams computation**

264 Phase diagrams in the CaO-(FeO)-MgO-SiO₂-H₂O-CO₂ (C(F)MS-H₂O-CO₂) system were
265 calculated using Perple_X (version 6.7.2, Connolly 1990, 2009) and the thermodynamic dataset and
266 equation of state for H₂O-CO₂ fluid of Holland and Powell (1998, revised 2004). Being impossible
267 at this stage to model all the complexities of UHP COH fluids due to the presence of silica and
268 alkalis as dominant solutes at UHP conditions, as well as of dissolved carbon species, our
269 calculations are limited to binary H₂O-CO₂ fluid (see e.g. Castelli et al., 2007) (note the different
270 notations: C(F)MS-COH, used to describe the relevant mineral assemblages, and C(F)MS-H₂O-
271 CO₂, used for the thermodynamic modelling). This also implies that it is not possible, at this stage,
272 to model processes different from the “classical” metamorphic reactions using the conventional
273 thermodynamic modelling approach.

274 For the calculation of the P/T - $X(\text{CO}_2)$ grid and mixed-volatile P - T projection in the CMS-H₂O-CO₂
275 system, the following solid end-members were considered: aragonite/calcite, brucite, dolomite,
276 diopside, forsterite, magnesite, quartz/coesite, talc and tremolite in addition to the binary H₂O-CO₂
277 fluid (Connolly and Trommsdorff, 1991).

278 For the calculation of the P/T - $X(\text{CO}_2)$ pseudosection in the CFMS-H₂O-CO₂ system, the following
279 solid solution models were used: amphibole (ideal model for tremolite), clinopyroxene, olivine and
280 dolomite (Holland and Powell 1998), in addition to the binary H₂O-CO₂ fluid. Calcite/aragonite and
281 quartz/coesite were considered as pure end-members. The bulk rock composition of sample DM675
282 has been calculated by combining the mineral proportions obtained from the modal estimate of

283 micro-XRF map with mineral chemistry acquired at WDS. In addition, as the studied sample shows
284 a banded structure, the bulk composition has been calculated for the olivine-rich layer with the most
285 abundant zoned dolomite crystals. Calculation of the bulk composition has been obtained starting
286 from the vol% of each mineral and from their compositions, and considering the molar volume of
287 each phase.

288

289 **AN OVERVIEW OF THE IMPURE CAL-DOL MARBLES**

290 In this section, an overview, not necessarily exhaustive, of the microstructures and mineral
291 compositions essential for the comprehension of the complex tectono-metamorphic evolution of the
292 impure calcite-dolomite marbles is reported.

293 The sampled impure calcite-dolomite marbles show a granoblastic, polygonal to mortar,
294 microstructure. Locally, the early-retrograde UHP regional foliation (see Fig. 1b) is recorded and,
295 depending on the local bulk composition (i.e., NKCFMAS-COH, (N)CFM(A)S-COH, or C(F)MS-
296 COH systems; see above and Table 1), is mainly defined by the preferred orientation of phengite,
297 Mg-chlorite, clinopyroxene and/or by silicate-rich layers wrapping around porphyroblastic
298 dolomite, clinopyroxene and olivine, or garnet, and/or zoisite (Fig. 2a-b; Fig. 3a-b). (Mg-)calcite
299 occurs in the rock matrix as weakly-deformed, coarse-grained relics with irregular grain boundaries,
300 or as medium-grained neoblasts. Locally, it includes vermicular inclusions of dolomite.

301 Considering the prograde- to early-retrograde evolution, at least four metamorphic events can be
302 recognized based on distinct silicate mineral assemblages (Fig. 4), which depend on local bulk
303 composition: i) *HT-LP* pre-Alpine event characterized by Ti-rich (Ti = 0.06 a.p.f.u.) andradite-rich
304 garnet (Fe^{3+} = 0.02 a.p.f.u.; Ca = 2.453 a.p.f.u.; Table 2; Fig. 2c-d), Fe-Na rich diopside with Ca-
305 tschermak component (Mg = 0.946-0.99 a.p.f.u., Al = 0.017-0.09 a.p.f.u., Fe_{tot} = 0.02-0.042 a.p.f.u.,
306 Na = 0.006-0.010 a.p.f.u.), forsterite with relatively (i.e. compared to the other forsterite
307 generations) low Mg# [$\text{Mg}/(\text{Mg}+\text{Fe}^{2+})$ = 0.983], pargasite, talc, ilmenite, and magnetite; ii) *HP*
308 Alpine prograde event (stages 2 or 3 in Fig. 1b) represented by Ti-Ca-poor (Ti = 0.01 a.p.f.u., Ca =

309 1.97 a.p.f.u.) almandine-rich garnet ($\text{Fe}^{2+} = 0.23$ a.p.f.u., Fig. 2d), Na-bearing diopside (Mg =
310 0.978-0.988 a.p.f.u., Al = 0.006 a.p.f.u., $\text{Fe}_{\text{tot}} = 0.011$ -0.019 a.p.f.u., Na = 0.004-0.006 a.p.f.u.),
311 forsterite with high Mg# (0.994), talc, phengite, zoisite, and titanite; iii) UHP peak event (stage 4 in
312 Fig. 1b) recorded by Ti-Fe-poor (Ti = 0.01 a.p.f.u., $\text{Fe}^{2+} = 0.21$ a.p.f.u.), grossular-rich (Ca = 2.07
313 a.p.f.u.) garnet (Fig. 2e), almost pure diopside (Mg = 0.987-1.010 a.p.f.u., Al \leq 0.003 a.p.f.u., $\text{Fe}_{\text{tot}} =$
314 0.001-0.008 a.p.f.u., Na \leq 0.001 a.p.f.u.), forsterite with high Mg# (0.993), phengite (Si = 3.53
315 a.p.f.u.), zoisite, and rutile; iv) UHP early-retrograde event locally developing the regional foliation
316 (stage 5 in Fig. 1b; Fig. 2a-b; Fig. 3a-b) and recorded by Na-bearing diopside (Mg = 0.991-1.000
317 a.p.f.u., Al \leq 0.001 a.p.f.u., $\text{Fe}_{\text{tot}} = 0.006$ -0.009 a.p.f.u., Na = 0.004 a.p.f.u., Fig. 2f), phengite,
318 forsterite with the highest Mg# (0.995), Mg-chlorite, Al-rich antigorite, phlogopite (Mg# = 0.92),
319 Na-bearing tremolite, Al-F-rich (Al = 0.18 a.p.f.u.; F = 0.106 a.p.f.u.) titanite. The late-retrograde
320 undifferentiated events (stages 6-11 in Fig. 1b) are represented by Mg-chlorite, antigorite, Mg-
321 hornblende, tremolite variably enriched in Na-Al-Fe (Fig. 2f), Na-bearing diopside (Mg = 0.990-
322 0.995 a.p.f.u., Al = 0.001-0.003 a.p.f.u., $\text{Fe}_{\text{tot}} = 0.002$ -0.011 a.p.f.u., Na = 0.002-0.003 a.p.f.u.),
323 forsterite, epidote *s.l.*, phlogopite, talc, and Al-F poor (Al = 0.10 a.p.f.u.; F = 0.065 a.p.f.u.) titanite.
324 In all impure calcite-dolomite marble types, dolomite occurs as sub-rounded pre-kinematic
325 porphyroblasts (Fig. 2a-c, g-h; Fig. 3) with curved, irregular or lobed grain boundaries, and it shows
326 a more rigid behaviour than calcite. Under both SEM (back-scattered electron images, BSE; Figs.
327 2c-d, e, g) and cathodoluminescence (CL; Fig. 2h; Figs. 3a, c-d), dolomite usually shows distinct
328 stages of growth, coupled with chemical variations and distinct mineral inclusions depending on the
329 local bulk composition and *P-T* conditions. Dol I constitutes a dark-gray (BSE), light- to medium-
330 red (CL) relic inner core rich in Cal component and locally including pre-Alpine mineral
331 assemblage (Figs. 2c-e, g-h; Figs. 3a, d). Dol II constitutes a dark-gray (BSE), medium-to-light red
332 (CL) outer core poor in Cal component and replacing, or concentrically overgrowing, the inner core
333 and locally including HP mineral assemblage (Fig. 2c-d, g-h, Fig. 3a, c-d). Dol III constitutes a
334 medium-gray (BSE), dark-red (CL) inner rim, with intermediate Cal-component, locally including

335 the UHP mineral assemblage (Fig. 2e), and asymmetrically overgrowing the partly reabsorbed core
336 (Figs. 2c, e, g-h; Fig. 3). Dol IV constitutes a light-gray (BSE), poorly luminescent (CL) outer rim
337 poor in Cal component, locally including early-retrograde mineral assemblages (Fig. 2g) and
338 overgrowing the inner rim in sharp discontinuity and locally without preserving its crystallographic
339 orientation (Figs. 2c-e, g-h; Fig. 3).

340

341 **SIMPLIFYING THE PROBLEM: AN EXAMPLE FROM THE $\text{CaO-(FeO)-MgO-SiO}_2\text{-COH}$ SYSTEM**

342 As evident from the previous section, the different local bulk compositions produce a large
343 variability in the silicate mineral assemblages referring to the same metamorphic stage. Their
344 correlation is nevertheless possible, comparing microstructural relationships (with respect to the
345 main foliation and/or to mineral inclusions) and/or trend of variation in mineral compositions, and
346 allows unambiguous interpretation of the prograde to early-retrograde evolution of dolomite (Fig.
347 4). The HP-UHP dolomite evolution can be more easily characterized and modelled in the
348 chemically-simple C(F)MS-COH system, well represented by the impure Cal-Dol marble sample
349 DM675 (Table 1).

350

351 **The $\text{Chl} \pm \text{Tr} \pm \text{Atg} \pm \text{Ol} \pm \text{Di}$ calcite-dolomite marble**

352 Sample DM675 is representative of mm-banded marble whose phase assemblages can be modelled
353 in the C(F)MS-COH system; each layer contains different modal amounts of calcite, dolomite,
354 clinopyroxene, and olivine (Fig. 5). In particular, the sample consists of Mg-calcite, porphyroblasts
355 of dolomite (Figs. 6a-c), porphyroblastic and neoblastic diopside (Figs. 6b-d), porphyroblastic and
356 neoblastic forsterite (Figs. 6a-b, d), and very minor retrograde antigorite (Figs. 6a, c-d), tremolite
357 and Mg-chlorite (Fig. 4).

358 Different generations of dolomite, diopside and forsterite have been recognized on the basis of
359 microstructural evidence (optical and CL microscopy) and mineral composition. Although BSE

360 images do not reveal a strong chemical zoning, WDS analyses reveal minor, but systematic,
361 changes in mineral compositions among the different generations.

362 In the zoned **dolomite** porphyroblasts, the four generations previously described (Fig. 4) are clearly
363 recognizable only under cathodoluminescence (Figs. 6a–b). The relict pre-Alpine inner core (Dol I)
364 is characterized by high CaCO₃ (Cal_{51.05-51.18}), low MgCO₃ (Mgs_{48.69}) and relatively low FeCO₃
365 (Sd_{0.08-0.17}) components (Figs. 7a-b and Table 3). The prograde outer core (Dol II: Cal_{49.94-}
366 _{50.13}Mgs_{49.72-49.92}Sd_{0.06-0.09}), concentrically overgrowing Dol I, shows a decrease in CaCO₃ and
367 FeCO₃ and an increase in MgCO₃. The peak inner rim overgrows Dol II with sharp and irregular
368 contacts (Figs. 6a–b) and has variable intermediate compositions (Dol III: Cal_{50.33-50.77}Mgs_{49.03-}
369 _{49.49}Sd_{0.11-0.19}). Early-retrograde Dol IV in the inner rim also shows irregular, re-entrant and sharp
370 contacts and, locally, different crystallographic orientation. It shows compositions similar to Dol II
371 (Dol IV: Cal_{49.97-50.07}Mgs_{49.80-49.81}Sd_{0.01-0.13}). MnO is present in all dolomite generations and ranges
372 from 0.001 to 0.097 wt%. The Mn/Fe ratio in the different dolomite generations (Fig. 7c) seems
373 correlated to the CL color, being broadly in the range: 0.2-0.5 (Dol I: light red), 0.6-0.7 (Dol II:
374 bright yellow) and 0.05-0.5 (Dol III: light-to-medium red). Data for Dol IV (dark red) are more
375 ambiguous, being the Mn/Fe ratio more variable.

376 **Clinopyroxene** is always an almost pure diopside. It occurs both as porphyroblasts, with preferred
377 dimensional orientation that locally define the early-retrograde regional foliation, and stubby
378 neoblasts. Under CL both porphyroblasts and neoblasts show a relatively irregular zoning that
379 corresponds to slight chemical variations. Five generations of diopside are recognized (Figs. 6b-d;
380 7d). The pre-Alpine Cpx I occurs as very rare relict cores, brown under CL, within the
381 porphyroblasts. Cpx I is Fe-Na bearing in composition (Mg = 0.946 a.p.f.u., Al = 0.017 a.p.f.u.,
382 Fe_{tot} = 0.042 a.p.f.u., Na = 0.010 a.p.f.u.; Table 2 and Fig. 7d) and it is the only generation of
383 diopside with significant amount of the Ca-tschermak component. The HP prograde Cpx II,
384 constituting the red (CL) core of porphyroblasts (Fig. 6d), has higher Mg and lower Na and Fe
385 contents (Mg = 0.978-0.988 a.p.f.u., Al = 0.006 a.p.f.u., Fe_{tot} = 0.011-0.019 a.p.f.u., Na = 0.004-

386 0.006 a.p.f.u.) with respect to Cpx I. The peak Cpx III, from yellow-orange to yellow-green under
387 CL, constitutes the core of neoblasts and inhomogeneous portions in the core of porphyroblasts
388 (Fig. 6d). Cpx III is a pure diopside ($Mg = 0.987-1.010$ a.p.f.u., $Al \leq 0.003$ a.p.f.u., $Fe_{tot} = 0.001-$
389 0.008 a.p.f.u., Na is below detection limit). Early-retrograde Cpx IV, yellow under CL, constitutes
390 the outer core of neoblasts and inhomogeneous portions in the rim of porphyroblasts (Fig. 6b, d). It
391 has Mg and Fe content similar to peak Cpx III, but it has slightly higher Na content ($Mg = 0.991-$
392 1.000 a.p.f.u., $Al \leq 0.001$ a.p.f.u., $Fe_{tot} = 0.006-0.009$ a.p.f.u., $Na = 0.004$ a.p.f.u.). Retrograde light
393 blue (CL) Cpx V asymmetrically overgrows Cpx IV in sharp discontinuity (Fig. 6b, d) and shows
394 lower Na content ($Mg = 0.990-0.995$ a.p.f.u., $Al = 0.001-0.003$ a.p.f.u., $Fe_{tot} = 0.002-0.011$ a.p.f.u.,
395 $Na = 0.002-0.003$ a.p.f.u.).

396 Under CL, forsterite is dark-red (Fig. 6a-b, d) and, as expected for this chemical system, evidence
397 for chemical zoning is apparently lacking in BSE images. However, at least four possible
398 generations of olivine, forsteritic in composition, seems to be present in textural equilibrium with
399 different dolomite and diopside generations (Fig. 4). Pre-Alpine Ol I is present as very rare relics
400 with relatively low Mg# (0.983) compared to the other forsterite generations. Pre-Alpine Ol I occurs
401 as slightly bright (CL) portions in the core of the porphyroblasts. More commonly, porphyroblasts
402 are characterized by $Mg\# = 0.993-0.994$, with the higher Mg# detected in the core (interpreted as
403 prograde Ol II; dark-red under CL; Fig. 6b) and lower Mg# detected in the rim (interpreted as
404 possible peak Ol III; darker-red under CL; Fig. 6b). The neoblasts in textural equilibrium with Cpx
405 IV (Fig. 6d) show the highest Mg# (0.995) and are interpreted as early-retrograde Ol IV.

406

407 **Thermodynamic modelling in the C(F)MS-H₂O-CO₂ system**

408 *P/T-X(CO₂)* petrogenetic grids and pseudosections (Fig. S1), and mixed-volatile *P-T* projection
409 (Fig. 8) have been modelled in the C(F)MS-H₂O-CO₂ system to predict the production vs.
410 consumption of dolomite through metamorphic reactions along the BIU prograde *P-T* path (Fig.
411 1b). More than 30 univariant and 20 invariant equilibria are modelled by the *P/T-X(CO₂)* grid (Fig.

412 S1a). Among them, only 8 univariant (i.e. curves 12-15, 17-18 and 26-27 in Fig. S1a) and two
413 invariant (i.e. points I1 and I13 in Fig. S1b) equilibria can be effectively “seen” by the studied
414 sample, as predicted by the P/T - $X(\text{CO}_2)$ pseudosection (Fig. S1b) calculated for the measured bulk
415 composition of sample DM675.

416 Invariant equilibria in the P/T - $X(\text{CO}_2)$ grid correspond to fluid-present univariant equilibria in the
417 P - T mixed-volatile projection of Fig. 8 (i.e. curves $i1$ to $i19$) (e.g. Baker et al., 1991; Carmichael,
418 1991; Connolly and Trommsdorff, 1991). This implies that the studied impure Cal-Dol marble
419 DM675 is sensitive to only two univariant equilibria (curves $i1$ and $i13$ in Fig. 8); both are Dol-
420 forming reactions. More in detail, the mixed-volatile P - T projection predicts that the first, and only,
421 prograde (1.7 GPa - 560°C) growth of dolomite in equilibrium with diopside and forsterite (i.e. the
422 observed assemblage Dol II + Cpx II + Ol II) occurred through the univariant reaction $i1$ (Fig. 8),
423 i.e. through the breakdown of antigorite + aragonite (i.e., $2.0 \text{ Arg} + 0.1 \text{ Atg} \rightarrow 1.0 \text{ Di} + 1.4 \text{ Fo} + 1.0$
424 $\text{Dol} + 3.1 F_{0.0003}$, where F is the fluid with composition expressed as $X(\text{CO}_2)$). In a H_2O - CO_2
425 saturated system, the subsequent HP-UHP prograde, peak and early-retrograde evolution of the
426 studied marble is entirely predicted in the Di + Fo + Dol + Arg stability field. Furthermore, along
427 the prograde and early-retrograde evolution, the composition of the fluid in equilibrium with this
428 mineral assemblage remains constant, because the P - T path is roughly parallel to the isopleths of
429 fluid composition (i.e. the red dotted lines in Fig. 8). This fluid is a dominantly aqueous H_2O - CO_2
430 fluid ($0.0003 < X(\text{CO}_2) < 0.0008$).

431 The observed microstructures combined with the results of phase diagram modelling strongly
432 suggest that the studied marble behaved as an internally buffered system during prograde and early-
433 retrograde evolution, i.e. the equilibrium mineral assemblage controlled the composition of the pore
434 fluid. Two evidences support this hypothesis: (i) the observed microstructures reflect the
435 isothermal/isobaric univariant assemblage Fo + Arg + Di + Dol (i.e. univariant equilibrium 15 in
436 Fig. S1a); for open system behaviour, isothermal/isobaric divariant assemblages would have been
437 instead observed (e.g. Trommsdorff, 1972; Hewitt, 1973; Kerrick, 1974; Rice & Ferry, 1982); (ii) if

438 significant fluid infiltration would have occurred (i.e. if the system was completely externally
439 buffered), either dolomite or olivine would have been completely consumed, depending on the
440 nature of the infiltrating fluid (i.e. either H₂O- or CO₂- rich; Fig. S1b).

441

442 **Fluid inclusion data**

443 Both UHP porphyroblastic and neoblastic Cpx III and IV include abundant primary multiphase
444 aqueous inclusions (Fig. 9). They are up to 10 μm long and 5 μm large, and show negative crystal
445 shape and crystallographic orientation. At room temperature the inclusions consist of H₂O (up to 40
446 vol% of the inclusion), locally biphasic (H₂O_L + H₂O_V; Fig. 9b). Under the optical microscope they
447 include apparently homogenous and birefringent crystals (Fig. 9c), but SEM-EDS qualitative
448 analyses reveal that these solid phases consists of an aggregate of Ca±Mg-carbonates and Cl-rich
449 hydrous Ca- and Mg-silicates. Micro-Raman spectra on these minerals, although showing broad
450 peaks, allow to recognize the carbonates as Mg-calcite (with typical peaks at 1089, 284 and 714 cm⁻¹;
451 Fig. 10a), and dolomite (characterized by peaks at 1098, 301, 177, 724 cm⁻¹). One of the silicates
452 results to be tremolite by the peaks at 676, 161, 126, 180, 224, 1063, 855, 303, 932, 417, 357 cm⁻¹,
453 and by the OH stretching vibration at 3674 cm⁻¹ (Fig. 10). The other silicate is talc, as testified by
454 the peaks at 197, 678, 506, 465, 368 cm⁻¹ (Fig. 10b). The intense peak at 3676 cm⁻¹ and the very
455 weak one at 3676 cm⁻¹, that are related to the OH stretching vibration of talc, arises from a large
456 band centred at about 3680 cm⁻¹ which is indicative for the presence of molecular water in its
457 crystallographic structure. More rarely, a small colourless (at the optical microscope) cube that does
458 not produce Raman spectrum (i.e., a chloride) is also visible within the inclusions.

459 The Raman spectral image of a primary fluid inclusions (Fig. 11) allows to visualize the distribution
460 of the solid phases within the inclusions and to qualitatively estimate their volume. Note that the
461 aqueous fluid in the inclusion has no significant Raman signal in the investigated region, and thus
462 does not interfere with the measurements. Mg-calcite constitutes large crystals that occupy about
463 65% of the inclusion volume, in association with a single small (about 5 vol%) crystal of dolomite.

464 Talc rich in Cl (SEM-EDS data) occurs as small crystals (about 10 vol%) around Mg-calcite. The
465 tremolite distribution is impossible to be obtained because its Raman bands are too close to those of
466 the host diopside or, for the OH band, to that of talc. However, it should occupy about 10% of the
467 inclusion volume.

468

469 **DISCUSSION: PREDICTED THERMODYNAMIC STABILITY VS. OBSERVED UNSTABLE BEHAVIOUR OF**

470 **DOLOMITE**

471 The sharp and irregular contacts observed between Dol II and Dol III, and between Dol III and Dol
472 IV suggest the succession of several episodes of corrosion/consumption and growth for the different
473 generations of dolomite. At least three different processes might explain the dolomite consumption
474 and growth at *HP/UHP* conditions and will be discussed in the following.

475

476 **Dolomite evolution by metamorphic reactions**

477 Although often overlooked (see the dissertation in Poli, 2014), compositional complexities in
478 dolomite have been reported in a few recent papers and mostly interpreted as the product of
479 prograde metamorphic reactions. Li et al. (2014) demonstrate that *UHP* zoned dolomite can record
480 evidence of the prograde *P-T* evolution of mafic eclogites from Tianshan, and of their interactions
481 with coexisting fluids. These authors describe metamorphic dolomite with zoning organized in both
482 normal and oscillatory patterns (Shore and Fowler, 1996), and show that this zoning is produced by
483 consecutive prograde metamorphic reactions. A paper by Mposkos et al. (2006) on *UHP* dolomitic
484 marbles from Rhodope proposes two hypotheses to explain the *UHP* Ca-rich composition (X_{MgCO_3}
485 = 0.34 – 0.43) observed at the dolomite rim or along cracks: i) it formed by high temperature ($T >$
486 850°C) metamorphic reaction involving the destabilization of Mg-calcite, to give aragonite and a
487 disordered dolomite able to incorporate high amounts of Ca (see also Franzolin et al., 2011); ii) it
488 formed by external influx of fluids leaching Mg from carbonates.

489 The irregular, re-entrant and sharp contacts observed in the zoned dolomite crystals investigated in
490 this study are very different from the dolomite zoning described by Li et al. (2014) or Mposkos et
491 al. (2006). Thermodynamic modelling in the C(F)MS-H₂O-CO₂ system (Figs. 8 and Fig. S1)
492 predicts a simple evolution for the BIU Cal-Dol marble and confirms that decarbonation reactions
493 do not occur during subduction, as also reported by previous studies (e.g., Molina and Poli, 2000;
494 Kerrick and Connolly, 2001 a, b; Castelli et al., 2007).

495 In particular, thermodynamic calculations predict the prograde growth of Dol II, in equilibrium with
496 Cpx II and Ol II, at 1.7 GPa and 560°C (i.e. at *P-T* conditions similar to those of stage 2; Fig. 1).
497 The Dol II -forming reaction involves the destabilization of aragonite coupled with antigorite
498 dehydration (univariant reaction *i1* in Fig. 8; isobaric/isothermal invariant point I1 in Fig. S1a) and
499 releases a dominantly aqueous fluid with $0.0003 < X(\text{CO}_2) < 0.0008$, which remains within the system.

500 The observed equilibrium assemblage further suggests that the system was internally buffered
501 during the whole prograde-to-peak and early-retrograde evolution (see above), i.e. it evolved along
502 the isobaric/isothermal univariant equilibrium 15 (Fig. S1a) during most of the prograde and early-
503 retrograde evolution. Internal buffering of fluid composition can be achieved either (i) in a
504 completely closed system or, (ii) in cases of limited fluid infiltration, i.e. intermediate conditions
505 between a complete internal buffering behaviour and a complete external buffering behaviour (e.g.
506 Greenwood, 1975; Rice and Ferry, 1982; Ferry, 1983; Ague and Rye, 1999). (i) If buffering
507 occurred in a completely closed system, the progress of reaction 15 was virtually null, i.e. the
508 prograde *HP-UHP* evolution occurred in the Di + Fo + Dol + Arg stability field without involving
509 any mineral production or consumption. The prograde *P-T* trajectory, in fact, is parallel to the
510 compositional isopleths of the fluid (Fig. 8): this means that, in order to maintain the equilibrium
511 between the mineral assemblage and the fluid, the reaction should not proceed, otherwise the fluid
512 composition would be shifted toward CO₂-richer compositions. Therefore, complete internal
513 buffering cannot explain either the consumption of Dol II and the growth of peak Dol III during the
514 prograde-to-peak evolution, or the consumption of Dol III and the growth of Dol IV during the

515 peak-to-early-retrograde evolution. (ii) The infiltration of small amounts of a CO₂-rich fluid (i.e.
516 $X(\text{CO}_2) > 0.0005$) or brines could have driven the isobaric/isothermal univariant reaction 15 ($2 \text{Fo} +$
517 $4 \text{Arg} + 2 \text{CO}_2 \rightarrow \text{Di} + 3 \text{Dol}$), favouring the formation of dolomite and diopside at the expenses of
518 forsterite and aragonite (now Mg-calcite). Such a process could explain the formation of both peak
519 Dol III + Cpx III and early-retrograde Dol IV + Cpx IV; however, it cannot explain neither the
520 formation of Ol III and Ol IV (microstructurally in equilibrium with Dol III and Dol IV,
521 respectively), nor the corrosion/consumption of Dol II and Dol III. Alternatively, the infiltration of
522 a H₂O-rich fluid (i.e. $X(\text{CO}_2) < 0.0005$) without dissolved salts could have driven the
523 isobaric/isothermal univariant reaction 15 in the reverse sense ($\text{Di} + 3 \text{Dol} \rightarrow 2 \text{Fo} + 4 \text{Arg} +$
524 2CO_2), enhancing the formation of forsterite and aragonite (now Mg-calcite) at the expenses of
525 diopside and dolomite. This process can explain the partial consumption of Dol II during the
526 prograde-to-peak evolution, and of Dol III during the peak-to-early-retrograde evolution. However,
527 it is not able to explain the growth of peak Dol III and Ol III, and of early-retrograde Dol IV and Ol
528 IV.

529 This implies that thermodynamic modelling fails in explaining the complexity of dolomite zoning
530 observed in the studied marbles. In fact, neither the consumption nor the growth of the observed
531 mineral assemblages (Dol III + Cpx III + Ol III; Dol IV + Cpx IV + Ol IV) result to have been
532 induced by metamorphic reactions. Because the thermodynamic modelling approach is not able to
533 explain the observed microstructures, a different process should be envisaged other than the
534 metamorphic reaction process, to explain the observed zoning of the dolomite crystals.

535

536 **Dolomite evolution by “dynamic wetting” of migrating grain boundaries**

537 The irregular, re-entrant and sharp contacts observed in the different dolomite generations from the
538 BIU impure marbles are similar to those described for calcite, replacing former aragonite, in Arg-
539 Dol-bearing calc-schists from Lago di Cignana (Reinecke et al., 2000), and interpreted as due to
540 lattice diffusion and interfacial mass transport linked with a heterogeneous distribution of fluid

541 (“dynamic wetting” of migrating grain boundaries; Reinecke et al., 2000). In the BIU marble, the
542 dolomite zoning cannot be ascribed only to this process because the presence of abundant,
543 crystallographically-oriented, primary multiphase (mainly silicates and carbonates + liquid)
544 aqueous inclusions in UHP diopside coexisting with dolomite indicates migration of carbonate-
545 bearing brines at least at the sample scale (i.e., well interconnected fluid films). Moreover, fluid
546 inclusions dropped from a fluid-filled moving grain boundary should be rounded and distributed
547 along the annealed grain-boundaries (e.g., Roedder, 1984; Craw and Norris, 1993; Schmatz and
548 Urai, 2010), whereas in the studied sample they are evenly distributed.

549

550 **Dolomite evolution by dissolution-precipitation processes**

551 A further process able to explain the observed microstructures in the studied BIU marbles is
552 dissolution-precipitation in aqueous fluids. The kinetics of dolomite dissolution is poorly known.
553 Experimental and thermodynamic studies on dolomite dissolution are commonly performed to
554 reproduce sedimentary conditions (e.g., Plummer and Busenberg, 1982). Experiments on
555 dissolution rates of dolomite at 25°C indicate that dissolved Ca is a strong inhibitor of dolomite
556 dissolution above neutral pH, whereas dissolved Mg has no effect on the dissolution rate
557 (Pokrovsky and Schott, 2001).

558 Experimental and theoretical studies performed on carbonate dissolution at high *P-T* conditions are
559 rare, and mainly focused on CaCO₃ (e.g., Fein and Walther, 1989; Newton and Manning, 2002;
560 Caciagli and Manning, 2003; Martinez et al., 2004; Dolejš and Manning, 2010; Manning et al.,
561 2013; Pan et al., 2013; Sanchez-Valle, 2013; Facq et al., 2014). Experimental data on calcite
562 dissolution during subduction suggest that the process is enhanced by: 1) the increase of both *P* and
563 *T* along a subduction geothermal gradient (Dolejš and Manning, 2010); 2) the presence of a saline
564 water (e.g., Newton and Manning, 2002), and in particular the presence of NO₃⁻, Cl⁻, SO₄²⁻ (in order
565 of increasing dissolution power; e.g., King and Putnis, 2013); 3) the decrease of pH (e.g., Manning
566 et al., 2013). At least two of these three factors enhancing carbonate dissolution-precipitation

567 processes occurred in the studied impure calcite-dolomite marbles: (1) they experienced a prograde
568 increase in both P and T ; (2) the fluid phase present at UHP conditions was a saline COH fluid.
569 From fluid inclusion study, the mineral phases within the inclusions (Mg-calcite + dolomite +
570 tremolite + talc) result to be the hydrous counterpart of the UHP mineral assemblage observed in
571 the studied sample. These minerals cannot be considered as incidentally trapped together with the
572 fluid inclusion because: i) they are present in all inclusions, and ii) both the relatively-broad Raman
573 peaks of minerals and the presence of molecular water in the crystallographic structure of talc (Fig.
574 10) indicate that they are poorly crystalline, and this is a typical feature of solids precipitated from
575 an aqueous fluid phase. In addition, the systematic occurrence of Cl in these hydrous minerals, and
576 the local occurrence of a small chloride within the fluid inclusions, indicate the presence of a saline
577 (fluid salinity > 26.3 wt% of NaCl_{eq}) aqueous solution in the inclusions. Thus, fluid inclusion data
578 indicate that the fluid phase present during the UHP evolution of the studied marble was a
579 dominantly aqueous, saline COH fluid, containing Ca, Mg, and Si as dissolved cations. These data
580 are in agreement with the thermodynamic modelling that predicts very low CO_2 content in the UHP
581 fluid phase. This COH fluid could have enhanced dissolution processes at UHP conditions,
582 explaining the irregular, re-entrant and sharp contacts observed in the zoned dolomite crystals.
583 The complex zoning of dolomite, diopside and forsterite could be therefore explained by protracted
584 episodes of dissolution and precipitation at HP/UHP conditions. More specifically, the following
585 dolomite evolution can be tentatively proposed:

586 (i) **growth of Dol II**: Dol II, concentrically overgrowing the pre-Alpine Dol I, formed through a
587 prograde metamorphic reaction involving the destabilization of aragonite and the dehydration of
588 antigorite (see previous discussion and Fig. 8). This reaction occurred at 1.7 GPa and 560°C
589 (i.e. at P - T conditions similar to those of stage 2 in Fig. 1b);

590 (ii) **consumption of Dol II**: during the subsequent increase in P - T conditions (from stage 2 to stage
591 4 in Fig. 1b), the brine previously produced by antigorite dehydration and still present in the
592 nearly closed system became able to dissolve Dol II, other than the metastable aragonite. In this

593 case the dissolution process could have been enhanced by the increase in both P and T
594 conditions;

595 (iii) **growth of peak Dol III**: the precipitation of peak Dol III (stage 4 in Fig. 1b) might have been
596 favoured by the attainment of over-saturation conditions of the fluid . The mechanism(s) for the
597 over-saturation at UHP peak still remain unclear, although it can be excluded that over-
598 saturation was induced by the decrease in fluid salinity, because of the nearly-closed behaviour
599 of the system. Previous thermodynamic studies on calcite solubility in aqueous fluids at HP
600 conditions (Dolejs and Manning, 2010) and pH measures on pure H_2O and on COH fluids in
601 equilibrium with a pelite up to $900^\circ C$ and 3 GPa (Galvez et al., 2015) were not able to predict
602 the attainment of the fluid over-saturation conditions required for carbonates precipitation
603 observed in the Dora-Maira sample. It is worth noting that, in the models of Galvez et al.
604 (2015), the UHP fluids are enriched in Si, Na, K, and Al, whilst in the studied marble the fluid
605 is a COH brine containing Ca, Mg, and Si. The presence of Ca and Mg and the lack of alkalies
606 as dissolved cations could have had a role, still unexplored, in the pH variations and, then, could
607 have possibly promoted the attainment of fluid over-saturation conditions and the consequent
608 precipitation of carbonates;

609 (iv) **consumption of Dol III**: although the system is no more in a subduction regime but in a very-
610 early decompressional evolution (from stage 4 to stage 5 in Fig. 1b), the residual fluid, having
611 lost part of its dissolved charge, is again a highly-reactive brine able to dissolve carbonates. In
612 particular, further dissolution can be facilitated by the increasing under-saturation of the
613 interfacial solution (Putnis and John, 2010; King and Putnis, 2013).

614 (v) **growth of Dol IV**: the subsequent precipitation of UHP Dol IV, might have been due again to
615 the attainment of fluid over-saturation conditions with respect to carbonates. In this case, fluid
616 over-saturation is probably caused by the abrupt P and T decrease, maybe coupled with the
617 increase in pH, during early exhumation (stage 5 in Fig. 1b).

618 Summing up, these dissolution-precipitation events likely continued during the whole prograde- to
619 early-retrograde evolution, as far as the *P-T* path remained within the dolomite + diopside stability
620 field.

621

622

IMPLICATIONS

623 Cathodoluminescence observations allowed to recognise a complex zoning pattern in dolomite, with
624 at least four growth shells. The irregular, re-entrant and sharp contacts between each growth shell
625 suggest a complex dolomite evolution, characterized by several episodes of dolomite consumption
626 and growth.

627 According to the thermodynamic modelling results, only the *HP* prograde growth of Dol II is due to
628 metamorphic reactions. On the contrary, the subsequent growth of *UHP* Dol III and Dol IV cannot
629 be induced by isochemical metamorphic reactions. Based on present data, the *UHP* growth of Dol
630 III and Dol IV, as well as the consumption of Dol II and Dol III, are interpreted as due to several
631 dissolution-precipitation episodes occurred in the presence of saline aqueous fluids. The *BIU P-T*
632 path and the occurrence of free high-saline fluids rich in Ca, Mg, Si represent favourable conditions
633 for: i) the inferred dissolution-precipitation processes of the stable dolomite in a nearly closed
634 system; ii) the possible migration of the dissolved carbonates, if the system would have been open
635 during subduction.

636 To our knowledge, this study presents the first evidence for *UHP* dissolution of dolomite in natural
637 samples. Therefore, it represents a contribution to the understanding of the *HP-UHP* evolution of
638 carbonates and to the understanding of the difference in solubility among dolomite and aragonite.

639 Concerning this second point, in fact, the presence of both calcite and dolomite in primary fluid
640 inclusions, with calcite volumetrically more abundant than dolomite (Fig. 11), suggests that: i) both
641 aragonite and dolomite are dissolved at *HP/UHP* condition, ii) aragonite seems to have a higher
642 solubility with respect to dolomite, and/or, iii) the CaCO_3 -component of dolomite has, maybe, a

643 higher solubility than its MgCO_3 -component (i.e., incongruent dissolution of dolomite; Busenberg
644 and Plummer, 1982).
645 Finally, the data reported in this study refer to a very simple chemical system [C(F)MS-COH], and
646 can therefore represent a useful starting point for: i) further experiments on dolomite dissolution at
647 HP-UHP conditions, which so far are still lacking, and ii) further studies on carbon production and
648 sequestration in ultramafic systems (i.e. the same C(F)MS-COH system).

649

650

ACKNOWLEDGEMENTS

651 S.F. thanks L. Martire and S. Cavagna for their assistance during CL sessions. We gratefully
652 acknowledge Roberto Compagnoni for being a constant source of inspiration and for sharing his
653 longstanding experience: we are indebted to him for most of our knowledge about the southern
654 Dora-Maira Massif. We thank P. Lanari and an anonymous reviewer for their comments that greatly
655 improved the manuscript, and D. Rubatto for editorial handling.

656 This work was financially supported by the Italian Prin project 2010PMKZX7 to D.C., S.F.,
657 M.L.F., C.G., by the University of Torino 2013 and 2014 funds (ex 60% grant) to D.C., S.F., C.G.,
658 and by the Austrian Science Found project P22479-N21 to A.P.. The micro-Raman equipment was
659 acquired by the Interdepartmental Center “G. Scansetti” for Studies on Asbestos and Other Toxic
660 Particulates with a grant from Compagnia di San Paolo, Torino.

661

662

REFERENCES CITED

663 Ague, J.J., and Nicolescu, S. (2014) Carbon dioxide released from subduction zones by fluid-
664 mediated reactions. *Nature Geoscience*, 7, 355-360.

665 Ague, J.J., and Rye, D.M. (1999) Simple models of CO_2 release from metacarbonates with
666 implications for interpretation of directions and magnitudes of fluid flow in the deep crust. *Journal*
667 *of Petrology*, 40, 1443-1462.

668 Baker, J., Holland, T., and Powell, R. (1991) Isograds in internally buffered systems without solid
669 solutions: principles and examples. *Contribution to Mineralogy and Petrology*, 106, 170-182.

670 Ballèvre, M. and Lagabrielle, Y (1994) Garnet in blueschist-facies marbles from the Queyras Unit
671 (Western Alps) – its occurrence and its significance. *Schweizerische Mineralogische und*
672 *Petrographische Mitteilungen*, 74, 203-212.

673 Buob, A., Luth, R.W., Schmidt, M.W., and Ulmer, P. (2006) Experiments on CaCO₃–MgCO₃ solid
674 solutions at high pressure and temperature. *American Mineralogist*, 91, 435–440.

675 Busenberg, E., and Plummer, L.N. (1982) The kinetics of dissolution of dolomite in CO₂-H₂O
676 systems at 1.5 to 65°C and 0 to 1 atm P_{CO₂}. *American Journal of Science*, 282, 45–78.

677 Caciagli, N.C., and Manning, C.E. (2003) The solubility of calcite in water at 5–16 kbar and 500–
678 800°C. *Contributions to Mineralogy and Petrology*, 146, 275–285.

679 Carmichael, D.M. (1991) Univariant mixed-volatile reactions: pressure–temperature phase
680 diagrams and reaction isograds. *Canadian Mineralogist*, 29, 741-754.

681 Carswell, D.A., and Van Roermund, H.L.M. (2005) On multi-phase mineral inclusions associated
682 with microdiamond formation in mantle-derived peridotite lens at Bardane on Fjærtøft, west
683 Norway. *European Journal of Mineralogy*, 17, 31-42.

684 Castelli, D. (1991) Eclogitic metamorphism in carbonate rocks: the example of impure marbles
685 from the Sesia-Lanzo Zone, Italian Western Alps. . *Journal of Metamorphic Geology*, 9, 61-77.

686 Castelli, D., Rolfo, F., Groppo, C., and Compagnoni, R. (2007) Impure marbles from the UHP
687 Brossasco-Isasca Unit (Dora-Maira Massif, western Alps): evidence for Alpine equilibration in the
688 diamond stability field and evaluation of the X_(CO₂) fluid evolution. *Journal of Metamorphic*
689 *Geology*, 25, 587-603.

690 Castelli, D., Compagnoni, R., Lombardo B., Angiboust S., Balestro G., Ferrando S., Groppo C.,
691 Hirajima T., Rolfo F. (2014): Crust-mantle interactions during subduction of oceanic & continental
692 crust. *Geological Field Trips*, 6, 73 pp.

693 Chopin, C. (1984) Coesite and pure pyrope in high-grade blueschists of the western Alps: a first
694 record and some consequences. *Contributions to Mineralogy and Petrology*, 86, 107-118.

695 Compagnoni, R., and Hirajima, T. (2001) Superzoned garnets in the coesite-bearing Brossasco-
696 Isasca Unit, Dora-Maira massif, Western Alps, and the origin of the whiteschists. *Lithos*, 57, 219-
697 236.

698 Compagnoni, R., Hirajima, T., and Chopin, C. (1995) Ultra-High-Pressure Metamorphic Rocks in
699 the Western Alps. In R.G. Coleman, and X. Wang, Eds. *Ultrahigh Pressure Metamorphism*, p. 206-
700 243. Cambridge University Press.

701 Compagnoni, R., Rolfo, F., Groppo, C., Hirajima, T., and Turello, R. (2004) Mapping of Alpine
702 rocks characterized by “HP” to “UHP” metamorphic overprint in the Southern Dora-Maira Massif
703 (Western Alps). In G. Pasquaré, C. Venturini, and G. Gropelli, Eds. *Mapping Geology in Italy*,
704 map 34, 287-294. APAT – Dipartimento Difesa del Suolo, Servizio Geologico d’Italia, Roma.

705 Compagnoni, R., Rolfo, F., Groppo, C., Hirajima, T., and Turello, R. (2012) Geological map of the
706 ultra-high pressure Brossasco-Isasca unit (Western Alps, Italy). *Journal of Maps*, 8, 465-472.

707 Connolly, J.A.D. (1990) Multivariable phase diagrams: an algorithm based on generalized
708 thermodynamics. *American Journal of Science*, 290, 666-718.

709 Connolly, J.A.D. (2005) Computation of phase equilibria by linear programming: a tool for
710 geodynamic modeling and its application to subduction zone decarbonation. *Earth and Planetary
711 Science Letters*, 236, 524-541.

712 Connolly, J.A.D. (2009) The geodynamic equation of state: what and how. *Geochemistry*
713 *Geophysic Geosystems*, 10, Q10014.

714 Connolly, J.A.D. and Trommsdorff, V. (1991) Petrogenetic grids for metacarbonate rocks:
715 pressure–temperature phase-diagrams for mixed-volatile systems. *Contribution to Mineralogy and*
716 *Petrology*, 108, 93-105.

717 Cook-Kollars, J., Bebout, G.E., Collins, N.C., Angiboust, S., and Agard, P. (2014) Subduction zone
718 metamorphic pathway for deep carbon cycling: I. Evidence from HP/UHP metasedimentary rocks,
719 Italian Alps. *Chemical Geology*, 386, 31-48.

720 Cossio, R., Borghi, A., and Ruffini, R. (2002) Quantitative modal determination of geological
721 samples based on X-ray multielemental map acquisition. *Microscopy and Microanalysis*, 8, 139-
722 149.

723 Craw, D., and Norris, J.R. (1993) Grain boundary migration of water and carbon dioxide during
724 uplift of garnet-zone Alpine Schist, New Zealand. *Journal of Metamorphic Geology*, 11, 371-378.

725 Dasgupta, R., and Hirschmann, M. M. (2010) The deep carbon cycle and melting in Earth's interior.
726 *Earth and Planetary Science Letters*, 298, 1–13.

727 Dasgupta, R., Hirschmann, M.M., and Dellas, N. (2005) The effect of bulk composition on the
728 solidus of carbonated eclogite from partial melting experiments at 3 GPa. *Contributions to*
729 *Mineralogy and Petrology*, 149, 288–305.

730 Davis, N.E., Newman, J., Wheelock, P.B., and Kronenberg, A.K. (2011) Grain growth kinetics of
731 dolomite, magnesite and calcite: a comparative study. *Physics and Chemistry of Minerals*, 38, 123–
732 138.

733 Di Vincenzo G., Tonarini S., Lombardo B., Castelli, D., and Ottolini, L. (2006) Comparison of
734 ^{40}Ar - ^{39}Ar and Rb-Sr data on phengites from the UHP Brossasco-Isasca Unit (Dora Maira Massif,
735 Italy): implications for dating white mica. *Journal of Petrology*, 47, 1439–1465.

736 Dobrzhinetskaya, L.F., Green, H.W., Bozhilov, N.K., Mitchell, T.E., and Dickerson, R.M. (2003)
737 Crystallization environment of Kazakhstan microdiamond: evidence from nanometric inclusions
738 and mineral associations. *Journal of Metamorphic Geology* 21, 425-437.

739 Dobrzhinetskaya, L.F., Wirth, R., and Green, H.W. (2007) A look inside of diamond forming media
740 in deep subduction zones. *Proceedings of the National Academy of Sciences*, 104, 9128–9132.

741 Dolejš, D., and Manning, C.E. (2010) Thermodynamic model for mineral solubility in aqueous
742 fluids: theory, calibration and application to model fluid-flow systems. *Geofluids*, 10, 20-40.

743 Droop, J.T.R. (2013) Paragonite in marbles from the Tauern Window, Austria: compositional and
744 thermobaric controls. *Lithos*, 162-163, 1-13.

745 Duchêne S, Blichert-Toft J, Luais B, Télouk P, Lardeaux JM, and Albarede F (1997) The Lu-Hf
746 dating of garnets and the ages of the Alpine high-pressure metamorphism. *Nature*, 387, 586-589.

747 Facq, S., Daniel, I., Montagnac, G., Cardon, H., and Sverjensky, D.A. (2014) In situ Raman study
748 and thermodynamic model of aqueous carbonate speciation in equilibrium with aragonite under
749 subduction zone conditions. *Geochimica et Cosmochimica Acta*, 132, 375-390.

750 Fein, J, and Walther, J.V. (1989) Calcite solubility and speciation in supercritical NaCl–HCl
751 aqueous fluids. *Contributions to Mineralogy and Petrology*, 103, 317–24.

752 Ferrando, S., Frezzotti, M.L., Dallai, L., and Compagnoni, R. (2005) Multiphase solid inclusions in
753 UHP rocks (Su-Lu, China): remnants of supercritical silicate-rich aqueous fluids released during
754 continental subduction. *Chemical Geology*, 223, 68-81.

755 Ferrando, S., Frezzotti, M.L., Petrelli, M., and Compagnoni, R. (2009) Metasomatism of continental
756 crust during subduction: the UHP whiteschists from the Southern Dora-Maira Massif (Italian
757 Western Alps). *Journal of Metamorphic Geology*, 27, 739-756.

758 Ferraris, C., Castelli, D., and Lombardo, B. (2005) SEM/TEM-AEM characterization of micro- and
759 nano-scale zonation in phengite from a UHP Dora-Maira marble: petrologic significance of
760 armoured Si-rich domains. *European Journal of Mineralogy*, 17, 453-464.

761 Ferry, J.M. (1983) On the control of temperature, fluid composition and reaction progress during
762 metamorphism. *American Journal of Science*, 283A, 201-232.

763 Franzolin, E., Schmidt, M.W., and Poli, S. (2011) Ternary Ca–Fe–Mg carbonates: subsolidus phase
764 relations at 3.5 GPa and a thermodynamic solid solution model including order/disorder.
765 *Contributions to Mineralogy and Petrology*, 161, 213-227.

766 Frezzotti, M.L., and Ferrando, S. (2015) The chemical behavior of fluids released during deep
767 subduction based on fluid inclusions. *American Mineralogist*, 100, 352-377.

768 Frezzotti, M.L., Huizenga, J.M., Compagnoni, R., and Selverstone, J. (2014) Diamond formation by
769 carbon saturation in C–O–H fluids during cold subduction of oceanic lithosphere. *Geochimica et*
770 *Cosmochimica Acta*, 143, 68-86.

771 Frezzotti, M.L., Selverstone, J., Sharp, Z.D., and Compagnoni, R. (2011) Carbonate dissolution
772 during subduction revealed by diamond-bearing rocks from the Alps. *Nature Geoscience*, 4, 703-
773 706.

774 Fu, B., Touret, J.L.R., and Zheng, Y.F. (2003) Remnants of pre-metamorphic fluid and oxygen-
775 isotopic signatures in eclogites and garnet clinopyroxenite from the Dabie-Sulu terranes, eastern
776 China. *Journal of Metamorphic Geology*, 21, 561-578.

777 Galvez, M.E., Manning, C.E., Connolly, J.A.D., and Rumble, D. (2015) The solubility of rocks in
778 metamorphic fluids: A model for rock-dominated conditions to upper mantle pressure and
779 temperature. *Earth and Planetary Science Letters*, 430, 486-498.

780 Gao, J., and Klemd, R. (2001) Primary fluids entrapped at blueschist to eclogite transition: evidence
781 from the Tianshan meta-subduction complex in northwestern China. *Contributions to Mineralogy
782 and Petrology*, 142, 1-14.

783 Gao, X.Y., Zheng, Y.F., Chen, Y.X., and Hu, Z. (2014) Composite carbonate and silicate
784 multiphase solid inclusions in metamorphic garnet from ultrahigh-P eclogite in the Dabie orogen.
785 *Journal of Metamorphic Geology*, 32, 961-980.

786 Gauthiez-Putallaz, L., Rubatto, D., and Hermann, J. (2016) Dating prograde fluid pulses during
787 subduction by in situ U–Pb and oxygen isotope analysis. *Contributions to Mineralogy and
788 Petrology*, 171, article 15, 20 pp.

789 Gebauer, D., Schertl, H.-P., Brix, M., and Schreyer, W. (1997) 35 Ma old ultrahigh-pressure
790 metamorphism and evidence for very rapid exhumation in the Dora Maira Massif, Western Alps.
791 *Lithos*, 41, 5-24.

792 Gorman, P.J., Kerrick, D.M., and Connolly J.A:D. (2006) Modeling open system metamorphic
793 decarbonation of subducting slabs. *Geochemistry, Geophysics, Geosystems*, 7, Q04007.

794 Grassi, D., and Schmidt, M.W. (2011) Melting of carbonated pelites at 8–13 GPa: generating K-rich
795 carbonatites for mantle metasomatism. *Contributions to Mineralogy and Petrology*, 162, 169-191.

796 Greenwood, H.J. (1975) Buffering of pore fluids by metamorphic reactions. *American Journal of
797 Science*, 275, 573–593.

798 Groppo, C., Castelli, D., and Rolfo, F. (2007a) HT, pre-Alpine relics in a spinel-bearing dolomite
799 marble from the UHP Brossasco-Isasca Unit (Dora-Maira Massif, western Alps, Italy). *Periodico di*
800 *Mineralogia*, 76, 155-168.

801 Groppo, C., Lombardo, B., Castelli, D., and Compagnoni, R. (2007b) Exhumation History of the
802 UHPM Brossasco-Isasca Unit, Dora-Maira Massif, as Inferred from a Phengite-Amphibole
803 Eclogite. *International Geology Review*, 49, 142-168.

804 Habermann, D., Neuser, R.D., and Richter, D.K. (1996) Low limit of Mn²⁺ -activated
805 cathodoluminescence of calcite: state of the art. *Sedimentary Geology*, 116, 13-24.

806 Habermann, D., Neuser, R.D., and Richter, D.K. (1996) REE-activated cathodoluminescence of
807 calcite and dolomite: high-resolution spectrometric analysis of CL emission (HRS-CL).
808 *Sedimentary Geology*, 101, 1-7.

809 Hammouda, T., Andrault, D., Koga, K., Katsura, T., and Martin, A. (2011) Ordering in double
810 carbonates and implications for processes at subduction zones. *Contributions to Mineralogy and*
811 *Petrology* 161, 439–450.

812 Hardie, L.A. (1987) Dolomitization: A critical view of some current views: *Journal of Sedimentary*
813 *Research*, 57, 166–183.

814 Hermann, J. (2003) Experimental evidence for diamond-facies metamorphism in the Dora Maira
815 massif. *Lithos*, 70, 163-182.

816 Hermann, J. (2003) Carbon recycled into the deep Earth: evidence from dolomite dissociation in
817 subduction-zone rocks: comment. *Geology*, 31, e4–e5.

818 Hewitt, D. A. (1973) The metamorphism of micaceous limestones from South-Central Connecticut.
819 *American Journal of Science*, 273A, 444-469.

820 Holland, T.J.B., and Powell, R. (1998) An internally consistent thermodynamic data set for phases
821 of petrologic interest. *Journal of metamorphic Geology*, 16, 309-343.

822 Hwang, S., Chu, H., Yui, T., Shen, P., Schertl, H.P., Liou, J.G., and Sobolev, S.V. (2006)
823 Nanometer-size P/K-rich silica glass (former melt) inclusions in microdiamond from the gneisses of
824 Kokchetav and Erzgebirge massifs: diversified characteristics of the formation media of
825 metamorphic microdiamond in UHP rocks due to host-rock buffering. *Earth and Planetary Science*
826 *Letters*, 243, 94-106.

827 Ishida, H., Ogasawara, Y., Ohsumi, K., and Saito, A. (2003) Two stage growth of microdiamond in
828 UHP dolomite marble from Kokchetav Massif, Kazakhstan. *Journal of Metamorphic Geology*, 21,
829 515-522

830 Jarc, S., and Zupancic, N. (2009) A cathodoluminescence and petrographical study of marbles from
831 the Pohorje area in Slovenia *Chemie der Erde*, 69, 75-80.

832 Kato, T., Enami, M., and Zhai, M. (1997) Ultra-high-pressure (UHP) marble and eclogite in the Su-
833 Lu UHP terrane, eastern China. *Journal of Metamorphic Geology*, 15, 169–182.

834 Kelemen, P.B., and Manning, C.E. (2015) Reevaluating carbon fluxes in subduction zones, what
835 goes down, mostly comes up. *Proceedings of the National Academy of Sciences*, 112, E3997-
836 E4006.

837 Kerrick, D. M. (1974). Review of mixed-volatile (H₂O-CO₂) equilibria. *American Mineralogist*, 59,
838 729-762.

839 Kerrick, D.M., and Connolly, J.A.D. (2001a) Metamorphic devolatilization of subducted marine
840 sediments and the transport of volatiles into the Earth's mantle. *Nature*, 411, 293–296.

841 Kerrick, D. M., and Connolly, J.A.D. (2001b) Metamorphic devolatilization of subducted oceanic
842 metabasalts: Implications for seismicity, arc magmatism and volatile recycling. *Earth Planetary*
843 *Science Letters*, 189, 19–29.

844 King, H.E., and Putnis, C.V. (2013) Direct observations of the influence of solution composition on
845 magnesite dissolution. *Geochimica et Cosmochimica Acta*, 109, 113-126.

846 Korsakov, A.V., De Gussem, K., Zhukov, V.P., Perraki, M., Vandenabeele, P., and Golovin, A.V.
847 (2009) Aragonite-calcite-dolomite relationships in UHPM polycrystalline carbonate inclusions from
848 the Kokchetav Massif, northern Kazakhstan. *European Journal of Mineralogy*, 21, 1301-1311.

849 Korsakov, A.V., and Hermann, J. (2006) Silicate and carbonate melt inclusions associated with
850 diamond in deeply subducted carbonate rocks. *Earth and Planetary Science Letters*, 241, 104-118.

851 Li, J.L., Klemd, R., Gao, J., and Meyer, M. (2014) Compositional zoning in dolomite from
852 lawsonite-bearing eclogite (SW Tianshan, China): Evidence for prograde metamorphism during
853 subduction of oceanic crust. *American Mineralogist*, 99, 206-217.

854 Liu, P., Wu, Y., Chen, Y., Zhang, J., and Jin, Z. (2015) UHP impure marbles from the Dabie
855 Mountains: Metamorphic evolution and carbon cycling in continental subduction zones. *Lithos*,
856 212-215, 280-297.

857 Luth, R.W. (2001) Experimental determination of the reaction aragonite + magnesite = dolomite at
858 5 to 9 GPa. *Contributions to Mineralogy and Petrology*, 141, 222-232.

859 Massonne, H.J. (2011) Phase relations of siliceous marbles at ultrahigh pressure based on
860 thermodynamic calculations: examples from the Kokchetav Massif, Kazakhstan and the Sulu
861 terrane, China. *Geological Journal*, 46, 114–125.

862 Manning, C.E., Shock, E.L., and Sverjensky, D.A. (2013) The chemistry of carbon in aqueous
863 fluids at crustal and upper-mantle conditions: experimental and theoretical constraints. *Reviews in*
864 *Mineralogy & Geochemistry*, 75, 109-148.

865 Martinez, I., Sanchez-Valle, C., Daniel, I. and Reynard, B. (2004) High-pressure and high-
866 temperature Raman spectroscopy of carbonate ions in aqueous solution. *Chemical Geology*, 207,
867 47–58.

868 Martinez, I., Zhang, J.Z., Reeder, R.J., 1996. In situ X-ray diffraction of aragonite and dolomite at
869 high pressure and high temperature; evidence for dolomite breakdown to aragonite and magnesite.
870 *American Mineralogist* 81, 611–624.

871 Molina, J-F., and Poli, S. (2000) Carbonate stability and fluid composition in subducted oceanic
872 crust: an experimental study on H₂O-CO₂-bearing basalts. *Earth Planetary Science Letters*, 176,
873 295–310.

874 Morlidge, M., Pawley, A., and Droop, G. (2006) Double carbonate breakdown reactions at high
875 pressures: an experimental study in the system CaO–MgO–FeO–MnO–CO₂. *Contributions to*
876 *Mineralogy and Petrology* 152, 365–373.

877 Mposkos, E., Baziotis, I., and Proyer, A. (2010): Metamorphic reprocessing of a serpentinized
878 carbonate-bearing peridotite after detachment from the mantle wedge: A P–T path constrained from
879 textures and phase diagrams in the system CaO–MgO–Al₂O₃–SiO₂–CO₂–H₂O. *Lithos*, 118, 349–
880 364.

881 Mposkos, E., Baziotis, I., Proyer, A., and Hoinkes, G. (2006) Dolomitic marbles from the
882 ultrahighpressure metamorphic Kimi complex in Rhodope, N.E. Greece. *Mineralogy and Petrology*,
883 88, 341-362.

- 884 Mposkos, E., Perraki, M., and Palikari, S. (2009) Single and multiphase inclusions in metapelitic
885 garnets of the Rhodope Metamorphic Province, NE Greece. *Spectrochimica Acta Part A: molecular*
886 *and biomolecular spectroscopy*, 73, 477-483.
- 887 Naemura, K., Hirajima, T., and Svojtka, M. (2009) The Pressure-Temperature Path and the Origin
888 of Phlogopite in Spinel-Garnet Peridotites from the Blanský Les Massif of the Moldanubian Zone,
889 Czech Republic. *Journal of Petrology*, 50, 1795-1827.
- 890 Newton, R.C., and Manning, C.E. (2002) Experimental determination of calcite solubility in H₂O-
891 NaCl solutions at deep crust/upper mantle pressures and temperatures: implications for metasomatic
892 processes in shear zones. *American Mineralogist*, 87, 1401-1409.
- 893 Ogasawara, Y., and Aoki, K. (2005) The role of fluid for diamond-free UHP dolomitic marble from
894 the Kokchetav Massif. *International Geology Review*, 47, 1178-1193.
- 895 Ogasawara, Y., Zhang, R.Y., and Liou, J.G. (1998) Petrogenesis of dolomitic marbles from
896 Rongcheng in the Su-Lu ultrahigh-pressure metamorphic terrane, eastern China. *Island Arc*, 7, 82-
897 97.
- 898 Omori, S., Liou, J.G., Zhang, R.Y., and Ogasawara, Y. (1998) Petrogenesis of impure dolomitic
899 marble from the Dabie Mountains, central China. *Island Arc*, 7, 98-114.
- 900 Pan, D., Spanu, L., Harrison, B., Sverjensky, D. A., and Galli, G. (2013) Dielectric Properties of
901 Water under Extreme Conditions and Transport of Carbonates in the Deep Earth. *Proceedings of*
902 *National Academy of Sciences*, 110, 6646-6650.
- 903 Philippot, P., Chevallier, P., Chopin, C., and Dubessy, J. (1995) Fluid composition and evolution in
904 coesite-bearing rocks (Dora-Maira massif, Western Alps): implications for element recycling during
905 subduction. *Contributions to Mineralogy and Petrology*, 121, 29-44.

906 Philippot, P., and Selverstone, J. (1991) Trace-element-rich brines in eclogitic veins: implications
907 for fluid composition and transport during subduction. *Contributions to Mineralogy and Petrology*,
908 106, 417-430.

909 Plummer, L.N., and Busenberg, E. (1982) The solubilities of calcite, aragonite and vaterite in CO₂-
910 H₂O solutions between 0 to 90 °C and an evaluation of the aqueous model for the system CaCO₃-
911 CO₂-H₂O. *Geochimica et Cosmochimica Acta*, 46, 1011-1040.

912 Pokrovsky, O.S., and Schott, J. (2001) Kinetics and mechanism of dolomite dissolution in neutral to
913 alkaline solutions revisited. *American Journal of Science*, 301, 597-626.

914 Poli, S. (2014) Dolomite discloses a hidden history of subducting slabs. *American Mineralogist*, 99,
915 pages 879-880.

916 Poli, S. (2015) Carbon mobilized at shallow depths in subduction zones by carbonatitic liquids.
917 *Nature Geoscience*, 8, 633-636.

918 Poli, S., Franzolin, E., Fumagalli, P., and Crottini, A. (2009) The transport of carbon and hydrogen
919 in subducted oceanic crust: An experimental study to 5 GPa. *Earth and Planetary Science Letters*,
920 278, 350-360.

921 Proyer, A., Mposkos, E., Baziotis, I., and Hoinkes, G. (2008) Tracing high-pressure metamorphism
922 in marbles: Phase relations in high-grade aluminous calcite-dolomite marbles from the Greek
923 Rhodope massif in the system CaO-MgO-Al₂O₃-SiO₂-CO₂ and indications of prior aragonite.
924 *Lithos*, 104, 119-130.

925 Proyer, A., Rolfo, F., Zhu, Y.F., Castelli, D., and Compagnoni, R. (2013) Ultrahigh-pressure
926 metamorphism in the magnesite + aragonite stability field: evidence from two impure marbles
927 from the Dabie-Sulu UHPM belt. *Journal of Metamorphic Geology*, 31, 35-48.

- 928 Putnis, A., and John, T. (2010) Replacement Processes in the Earth's Crust. *Elements*, 6, 159-164.
- 929 Reinecke, T., Bernhardt, H.-J., and Wirth, R. (2000) Compositional zoning of calcite in a high-
930 pressure metamorphic calc-schist: clues to heterogeneous grain-scale fluid distribution during
931 exhumation. *Contrib. Mineral. Petrol.*, 139, 584-606.
- 932 Rice, J.M., and Ferry, J. M. (1982) Buffering, infiltration, and control of intensive variables during
933 metamorphism. *Reviews in Mineralogy*, 10, 263-326.
- 934 Roedder, E. (1984) Fluid inclusions. *Review in Mineralogy*, 12, p. 678. Mineralogical Society of
935 America, Washington.
- 936 Rubatto, D., and Hermann, J. (2001) Exhumation as fast as subduction? *Geology*, 29, 3-6.
- 937 Sanchez-Valle, C. (2013) Structure and thermodynamics of subduction zone fluids from
938 spectroscopic studies. *Reviews in Mineralogy and Geochemistry*, 76, 265–309.
- 939 Sanchez-Valle, C., Mantegazzi, D., and Driesner, T. (2013) Thermodynamics of carbon-bearing
940 fluids and oxidised carbon speciation equilibria in subduction zone fluids. *Goldschmidt 2013*
941 *Conference Abstract*, 2125.
- 942 Sato, K., and Katsura, T. (2001) Experimental investigation on dolomite dissociation into aragonite
943 + magnesite up to 8.5 GPa. *Earth and Planetary Science Letters*, 184, 529–534.
- 944 Schertl, H.P., Neuser, R.D., Sobolev, N.V., and Shatsky, V.S. (2004) UHP-metamorphic rocks from
945 Dora Maira/Western Alps and Kokchetav/Kazakhstan: new insights using cathodoluminescence
946 petrography. *European Journal of Mineralogy*, 16, 49-57.
- 947 Schmatz, J., and Urai, J.L. (2010) The interaction of fluid inclusions and migrating grain boundaries
948 in a rock analogue: deformation and annealing of polycrystalline camphor–ethanol mixtures.
949 *Journal of Metamorphic Geology*, 28, 1-18.

950 Shore, M., and Fowler, A.D. (1996) Oscillatory zoning in minerals: a common phenomenon. The
951 Canadian Mineralogist, 34, 1111-1126.

952 Schmidt, M.W., and Poli, S. (2014) Devolatilisation during subduction. Treatise on Geochemistry,
953 4, 669-701.

954 Selverstone, J., Franz, G., Thomas, S., and Getty, S. (1992) Fluid variability in 2 GPa eclogites as
955 indicator of fluid behaviour during subduction. Contributions to Mineralogy and Petrology, 112,
956 341-357.

957 Smit, M.A., Bröcker, M., Scherer, E.E. (2008) Aragonite and magnesite in eclogites from the Jæren
958 nappe, SW Norway: disequilibrium in the system $\text{CaCO}_3\text{-MgCO}_3$ and petrological implications.
959 Journal of Metamorphic Geology, 26, 959-979.

960 Svensen, H., Jamtveit, B., Yardley, B.W.D., Engvik, A.K., Austrheim, H., and Broman, C. (1999)
961 Lead and bromine enrichment in eclogite-facies fluids: extreme fractionation during lower-crustal
962 hydration. Geology, 27, 467-470.

963 Trommsdorff, V. (1972) Change in T-X during metamorphism of siliceous rocks of the Central
964 Alps. Schweizerische Mineralogische und Petrographische Mitteilungen, 52, 567-571.

965 Tumati, S., Fumagalli, P., Tiraboschi, C., and Poli, S. (2013) An Experimental Study on COH-
966 bearing Peridotite up to 3.2 GPa and Implications for Crust-Mantle Recycling. Journal of Petrology,
967 54, 453-479.

968 Vaggelli, G., Borghi, A., Cossio, R., Fedi, M., Giuntini, L., Lombardo, B., Marino, A., Massi, M.,
969 Olmi, F., and Petrelli, M. (2006) Micro-PIXE analysis of monazite from the Dora Maira Massif,
970 Western Italian Alps. Microchimica Acta, 155, 305-311.

971 Wang, X.M., and Liou, J.G. (1993) Ultra-high-pressure metamorphism of carbonate rocks in the
972 Dabie Mountains, central China. *Journal of Metamorphic Geology* 11, 575–588.

973 Whitney, D.L., and Evans, B.W. (2010) Abbreviations for names of rock-forming minerals.
974 *American Mineralogist*, 95, 185-187.

975 Zhang, L., Ellis, D.J., Arculus, R.J., Jiang, W., and Wei, C. (2003). ‘Forbidden zone’ subduction of
976 sediments to 150 km depth — the reaction of dolomite to magnesite + aragonite in the UHPM
977 metapelites from western Tianshan, China. *Journal of Metamorphic Geology*, 21, 523–529.

978 Zhu, Y.F., and Ogasawara, Y. (2002) Carbon recycled into deep Earth: evidence from dolomite
979 dissociation in subduction-zone rocks. *Geology*, 30, 947–950.

980

981

FIGURE CAPTIONS

982 **Figure 1: (a)** Simplified geological map of the coesite-bearing Brossasco-Isasca Unit (modified
983 from Compagnoni et al., 2004 and Castelli et al., 2007). Undifferentiated units: graphite-rich schists
984 and metaclastics of the epidote-blueschist facies “Pinerolo Unit”; “San Chiaffredo Unit” and
985 “Rocca Solei Unit”, with pre-Alpine basement rocks overprinted by Alpine quartz-eclogite facies
986 metamorphism. The white stars show the two locations of the studied marbles. The inset shows the
987 location of the Southern Dora-Maira Massif within a simplified tectonic sketch-map of the Western
988 Alps. Helvetic-Dauphinois domain: MB, Mont Blanc-Aiguilles-Rouges. Penninic domain: SB,
989 Grand St. Bernard Zone; MR, Monte Rosa; GP, Gran Paradiso; DM, Dora-Maira; V, Valosio; PZ,
990 Piemonte zone of calcschists with meta-ophiolites. Austroalpine Domain: DB, Dent Blanche nappe;
991 ME, Monte Emilius klippe; SZ, Sesia-Lanzo zone; SA, Southern Alps; EU, Embrunais-Ubaye
992 flysch nappe; PF, Penninic thrust front; CL, Canavese line. **(b)** Variscan and Alpine P - T (- t) paths of
993 the Brossasco-Isasca Unit inferred from previous studies (see for comparison Castelli et al., 2014).
994 Open circles labelled 1 to 11 represent the Alpine metamorphic stages inferred from different

995 lithologies (whiteschist, marble, eclogite, calc-silicate rocks, orthogneiss) discussed in the text. Data
996 of stage 1 are inferred from Compagnoni and Hirajima (2001) and Ferrando et al. (2009); those of
997 stage 2 from Ferrando et al. (2009); those of stage 3 from Ferraris et al. (2005), Di Vincenzo et al.
998 (2006), Ferrando et al. (2009), Gauthiez-Putallaz et al (2016); those of stage 4 from Gebauer et al.
999 (1997), Hermann (2003), Vaggelli et al. (2006); Ferrando et al. (2009), Gauthiez-Putallaz et al
1000 (2016); those of stage 5 from Rubatto and Hermann (2001), Hermann (2003), Ferraris et al. (2005);
1001 Di Vincenzo et al. (2006), Castelli et al. (2007), Groppo et al. (2007b), Ferrando et al. (2009); those
1002 of stage 6 from Hermann (2003), Ferraris et al. (2005), Di Vincenzo et al. (2006); those of stage 7
1003 from Hermann (2003), Di Vincenzo et al. (2006), Castelli et al. (2007), Groppo et al. (2007b); those
1004 of stage 8 from Ferraris et al. (2005), Di Vincenzo et al. (2006), Castelli et al. (2007), Groppo et al.
1005 (2007b); those of stage 9 from Hermann (2003), Di Vincenzo et al. (2006), Castelli et al. (2007),
1006 Groppo et al. (2007b); those of stage 10 from Rubatto and Hermann (2001), Di Vincenzo et al.
1007 (2006), Castelli et al. (2007); those of stage 11 from Rubatto and Hermann (2001), Ferraris et al.
1008 (2005), Di Vincenzo et al. (2006), Castelli et al. (2007).

1009 **Figure 2:** Representative microstructures of calcite-dolomite marbles referring to the (N)CFM(A)S-
1010 COH (a) and NKCFMAS-COH (b-h) systems. **(a)** Amphibole and chlorite poorly defines an early-
1011 retrograde UHP regional foliation. Porphyroblasts of stretched dolomite are also evident. Sample
1012 DM1657, crossed polarized light (XPL). **(b)** Porphyroclastic Na-diopside, including prograde
1013 phengite, and dolomite are wrapped around by the early-retrograde UHP regional foliation defined
1014 by phengite and neoblastic Na-diopside. Sample DM1649, XPL. **(c)** Back scattered (BSE) image of
1015 a zoned dolomite with a dark-grey inner core (Dol I), including pre-Alpine andraditic garnet and
1016 diopside with Ca-tschermak component, overgrown by a dark-gray outer core (Dol II) and a
1017 medium-gray inner rim (Dol III). A light-gray outer rim (Dol IV) overgrows previous dolomite
1018 generations. Sample ADM17, back scattered image (BSE). **(d)** Dark-grey Dol II outer core with
1019 inclusions of zoned garnet. The pre-Alpine andradite-rich core is rimmed by the HP prograde
1020 almandine-rich rim. Both of them includes calcite. The medium-gray inner rim (Dol III) and the

1021 light-gray outer rim (Dol IV) of dolomite are also recognizable. Sample ADM17, BSE. **(e)**
1022 Medium-gray Dol III inner rim with an inclusion of UHP grossular-rich garnet. The picture also
1023 shows the dark-grey outer core (Dol II) and the light-grey outer rim (Dol IV) of dolomite. Sample
1024 DM1636, BSE. **(f)** Relict of neoblastic early-retrograde UHP Na-bearing diopside partly replaced by
1025 late-retrograde tremolite. Sample DM1631, XPL. **(g)** BSE image of zoned dolomite porphyroblasts
1026 showing relict dark-gray inner core (Dol I) concentrically overgrown by dark-gray HP Dol II outer
1027 core. The medium-grey UHP inner rim (Dol III) overgrows the partly reabsorbed core. The light-
1028 grey early retrograde outer rim (Dol IV), in equilibrium with tremolite, overgrows the previous,
1029 partly reabsorbed, dolomite generations. Inset not in scale. Sample ADM17. **(h)**
1030 Cathodoluminescence (CL) image of zoned dolomite porphyroblasts in which the light-red Dol I,
1031 the medium-red Dol II, the dark-red Dol III and the poorly luminescent Dol IV generations show
1032 the same microstructural relationships observed in Figs. 2c, d,e, g. Inset not in scale. Sample
1033 DM1657.

1034 **Figure 3:** Representative microstructures of calcite-dolomite marbles referring to the C(F)MS-COH
1035 system as recognized in CL and BSE. **(a)** The foliation is defined by not-luminescent Mg-chlorite
1036 that wraps around dolomite porphyroclasts characterized by four stages of growth. Inset not in
1037 scale. Sample DM1638, CL. **(b)** Dolomite porphyroclast wrapped around by flakes of Mg- chlorite;
1038 both are cut by rare antigorite. DM1638, BSE **(c)** Calcite-dolomite marble with a granoblastic
1039 structure. The porphyroclastic dolomite shows three stages of growth and not-luminescent Ca-
1040 amphiboles are also present. Sample DM1657, CL. **(d)** A dolomite porphyroclast is characterized
1041 by four stages of growth. Not-luminescent Mg-chlorite locally defines the main foliation. Sample
1042 DM1170, CL.

1043 **Figure 4:** Metamorphic evolution of the impure calcite-dolomite marbles from the BIU; mineral
1044 assemblages referring to the (N)CFM(A)S-COH and NKCFMAS-COH systems are reported in dark
1045 gray, those referring to the C(F)MS-COH system are reported in light gray.

1046 **Figure 5:** Major elements μ -XRF map of the whole thin section from sample DM675. The marble
1047 shows a banded fabric: each layer contains different modal amounts of calcite, dolomite,
1048 clinopyroxene, and olivine in textural equilibrium. The white dashed box refers to the olivine-rich
1049 level that was considered for the estimate of the bulk composition to be used in the pseudosection
1050 modelling.

1051 **Figure 6:** Representative microstructures from the chemically simple sample DM675 (C(F)MS-
1052 COH system), as recognized in cathodoluminescence (CL) and SEM (BSE). **(a)** The foliation is
1053 defined by the preferred dimensional orientation of zoned dolomite. Porphyroblastic forsterite is
1054 partly retrogressed to antigorite along cracks. CL. **(b)** Neoblastic forsterite and yellow Cpx IV are
1055 included in Dol IV. Yellow Cpx IV, locally rimmed by light-blue Cpx V, growths around
1056 porphyroblastic forsterite. CL. **(c)** Porphyroblastic dolomite includes Cpx III in the core (Dol III)
1057 and Cpx IV in the rim (Dol IV). BSE. **(d)** Diopside occurs as zoned porphyroblasts, showing
1058 dimensional preferred orientation along the regional foliation, and stubby zoned neoblasts.
1059 Porphyroblastic forsterite partly retrogressed to antigorite is also present. CL

1060 **Figure 7 (a-c)** Dolomite composition plotted in the CaCO_3 vs MgCO_3 **(a)**, FeCO_3 **(b)**, and
1061 MnO/FeO **(c)** diagrams. **(d)** Clinopyroxene composition plotted in the Mg vs Na diagram. WDS
1062 data from sample DM675.

1063 **Figure 8:** Mixed-volatile P - T projection calculated in the system CMS- H_2O - CO_2 . The univariant
1064 reactions “seen” by the studied sample DM675 and relevant for the prograde P - T path of the BIU
1065 (blue dotted line; see Fig. 1b) are reported in black, whereas the others (unlabeled) are reported in
1066 grey (see also Fig. S1). Large black dots are invariant points for the relevant reactions. The yellow
1067 field is the stability field of the Arg + Dol + Di + Fo + F assemblage, i.e. the assemblage observed
1068 in sample DM675. The studied marble is sensitive to only two Dol-forming univariant reactions,
1069 which are reported in red ($i1$ and $i13$). Fluid composition varies along each fluid-present univariant
1070 curve. Dotted red lines are isopleths of fluid (F) composition ($X\text{CO}_2$) in the Arg + Dol + Di + Fo +
1071 F stability field; the small red dots indicate the variation in fluid composition.

1072 **Figure 9:** Microphotographs showing primary fluid inclusions in diopside. **(a)** Primary fluid
1073 inclusions containing high birefringent solids are included in both porphyroclastic and neoblastic
1074 Cpx III. Sample DM675, XPL. **(b)** Detail of Cpx III including a primary fluid inclusion that
1075 consists of an aggregate of calcite + dolomite + tremolite + talc and an aqueous fluid phase (liquid
1076 and vapour). Sample DM675, PPL. **(c)** Detail of Cpx III including primary fluid inclusions that
1077 consists mainly of an aggregate of high birefringent solids (calcite + dolomite + tremolite + talc).
1078 Sample DM675, XPL.

1079 **Figure 10:** Raman spectra of solids within primary multiphase aqueous inclusions in diopside.
1080 Sample DM675. **(a)** Raman spectrum of mixed Mg-calcite + tremolite + host diopside. The broad
1081 peaks related to the minerals in the inclusion indicate their poor crystallinity. **(b)** Raman spectrum
1082 of mixed talc + tremolite + host diopside. The 3676 cm^{-1} peak, related to the OH bonds of talc,
1083 arises from a large band, suggesting the presence of molecular water in the crystallographic
1084 structure. The peak related to OH bonds of tremolite (see Fig. 9a) is not visible because of the very
1085 low intensity of the mineral in this site.

1086 **Figure 11:** **(a)** Photomicrograph of the mapped primary multiphase aqueous inclusion; the mapped
1087 area is $16 \times 16\ \mu\text{m}$. Sample DM 675, XPL. **(b-d)** Raman spectral images, respectively, of Mg-
1088 calcite (1089 cm^{-1}), talc (190 cm^{-1}), and dolomite (303 cm^{-1}) distribution in the fluid inclusion. The
1089 color intensity of the daughter minerals (from black to white) reflects the increase in the intensity of
1090 the Raman band.

1091 **Table 1:** samples of impure calcite-dolomite marbles referring to the C(F)M(A)S-COH,
1092 (N)CFM(A)S-COH, and NKCFMAS-COH systems. Wm = white mica

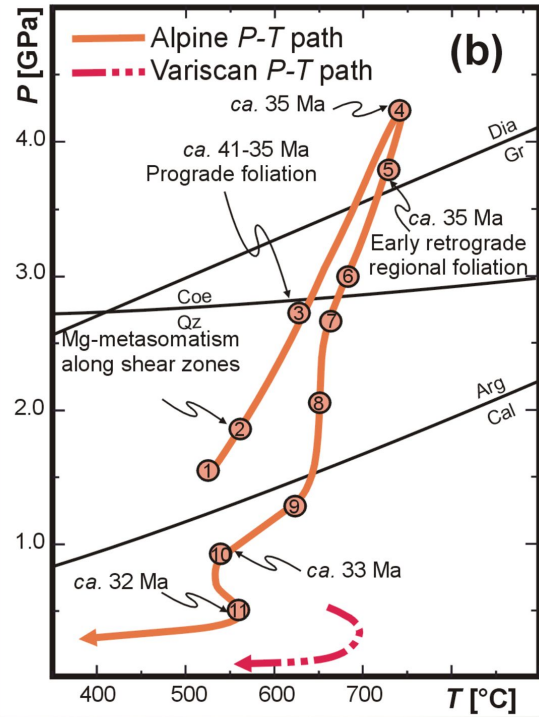
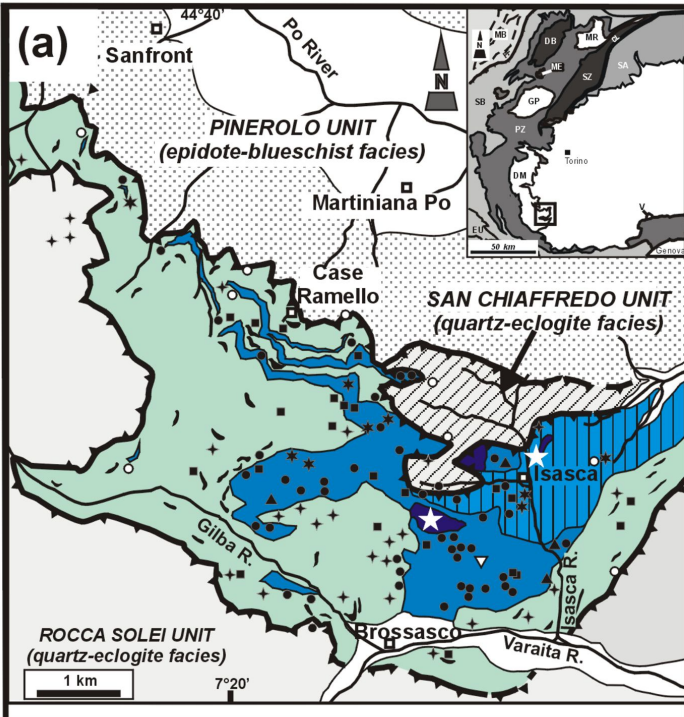
1093 **Table 2:** representative chemical composition of silicates from the impure calcite-dolomite marbles.
1094 EDS-WDS* = WDS data for Na and F; Fe_2O_3^* = calculated; “-“ not measured; b.d.l. = below
1095 detection limit; $\text{Mg}\# = \text{Mg}/(\text{Mg}+\text{Fe}^{2+})$

1096 **Table 3:** representative chemical composition of dolomite from sample DM675. b.d.l. = below
1097 detection limit

1098 **Figure supp mat 1: (a)** P/T - $X(\text{CO}_2)$ phase diagram section in the system CMS-H₂O-CO₂,
1099 calculated for the prograde P - T path of the BIU (Fig. 1b). Product assemblages on the right side of
1100 reactions; the isobaric/isothermal univariant reactions “seen” by the studied sample DM675 are
1101 reported in red. Qz/Coe-bearing equilibria are not numbered. Large black points are
1102 isobaric/isothermal invariant points; the fluid-present isobaric/isothermal invariant points
1103 correspond to univariant curves in the P - T mixed volatile projection of Fig. 7. **(b)** P/T - $X(\text{CO}_2)$
1104 pseudosection calculated for sample DM675 (bulk composition in mol%) in the system CFMS-
1105 H₂O-CO₂ for the prograde P - T path of the BIU. White (i.e. 5 mineral phases), light-grey (4 mineral
1106 phases) and dark-grey (3 mineral phases) fields are di-, tri- and quadri-variant fields, respectively.
1107 The narrow isobaric/isothermal 3-phases fields correspond to the isobaric/isothermal univariant
1108 reactions in (a). The stable assemblage Ol + Cpx + Dol + Arg is modelled by the narrow 4-phases
1109 field labelled in red.

1110 **Table supp mat 1:** chemical composition of silicates from the impure calcite-dolomite marbles.
1111 EDS-WDS* = WDS data for Na and F; Fe₂O₃* = calculated; "-" = not measured; b.d.l. = below
1112 detection limit.

1113



BROSSASCO-ISASCA UNIT (coesite-eclogite facies)

Polymetamorphic Complex

Paraschists with Coe-eclogite and marbles

Main marble lenses

Phengite-rich gneiss

Monometamorphic Complex

Augen gneiss with pyrope-bearing whiteschist layers

- ✦ relict Permian granitoid
- ▽ relict regionally metamorphosed Variscan paraschist
- ▲ relict thermally metamorphosed Variscan paraschist
- ★ small marble lenses
- fresh eclogite
- retrogressed eclogite
- Ky + Jd assemblages

Figure 1

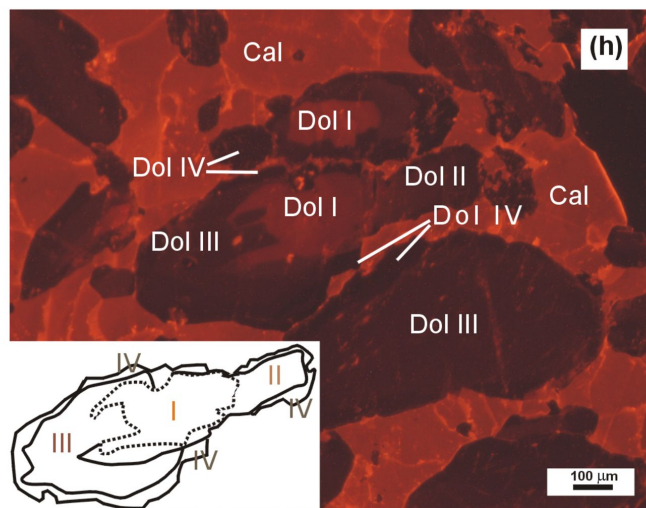
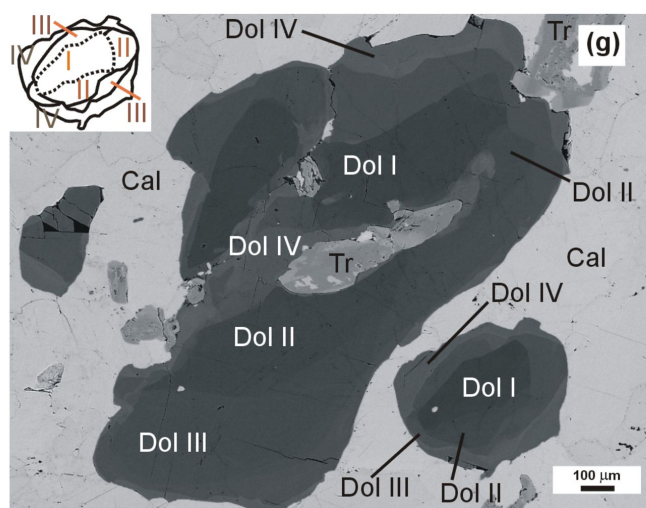
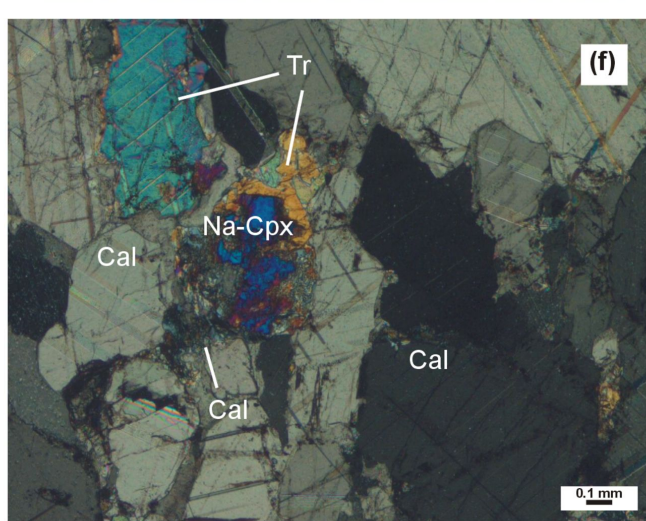
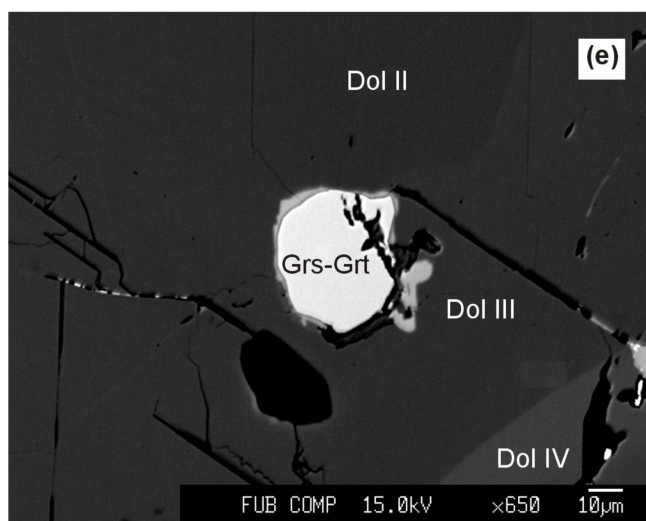
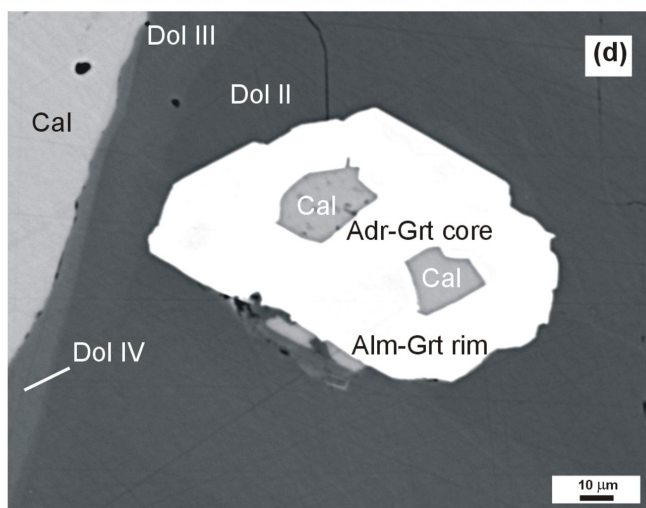
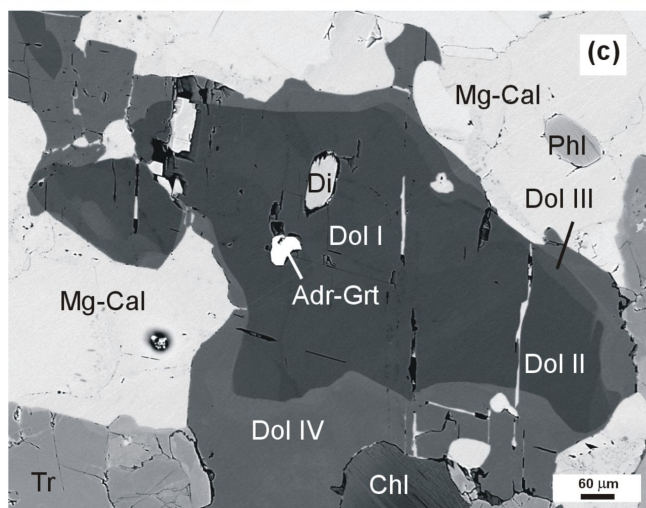
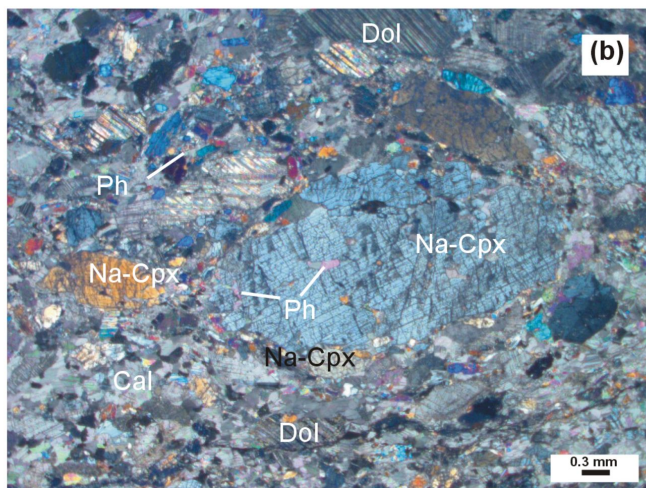
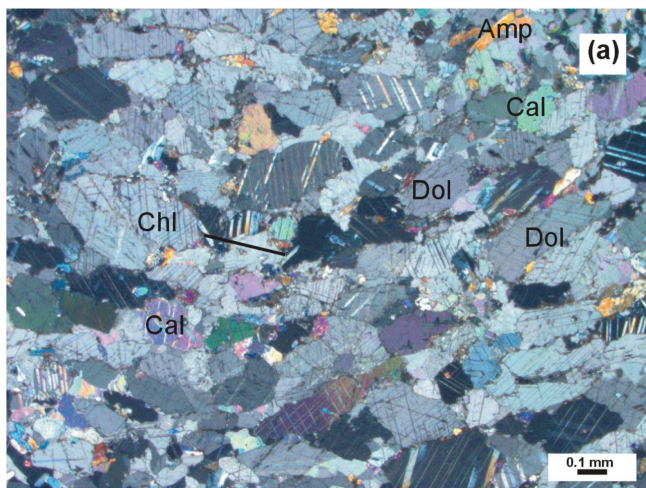


Figure 2

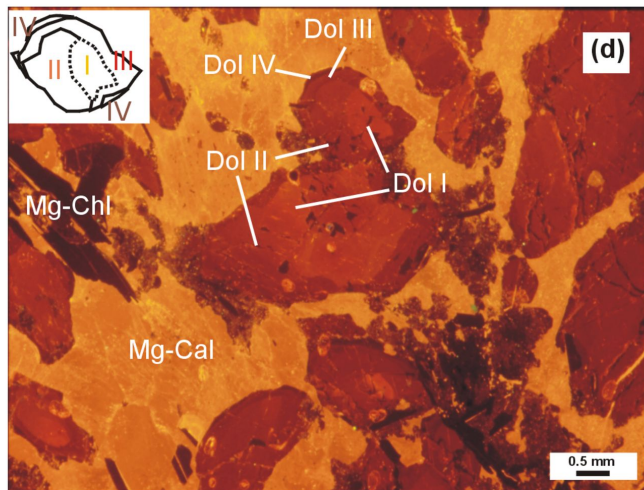
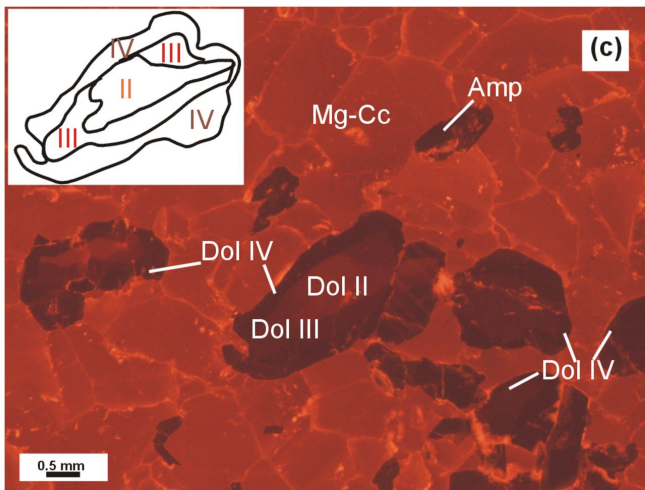
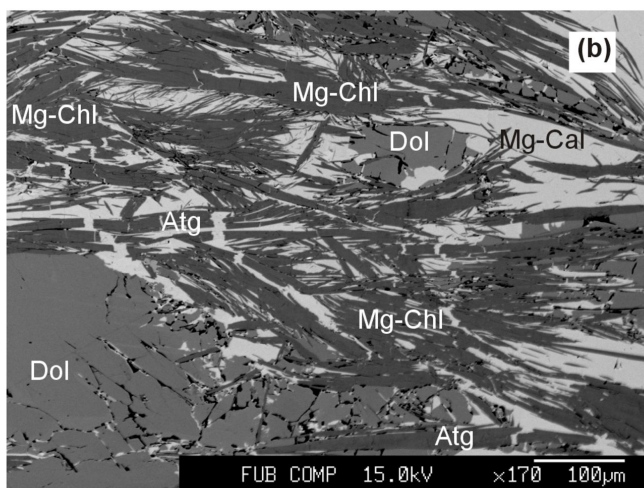
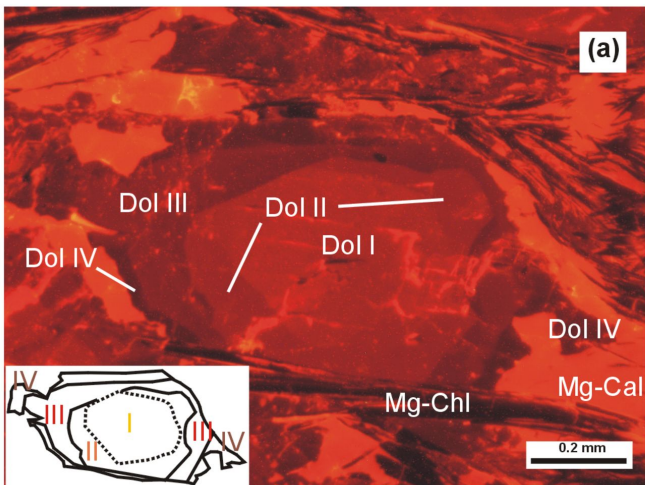


Figure 3

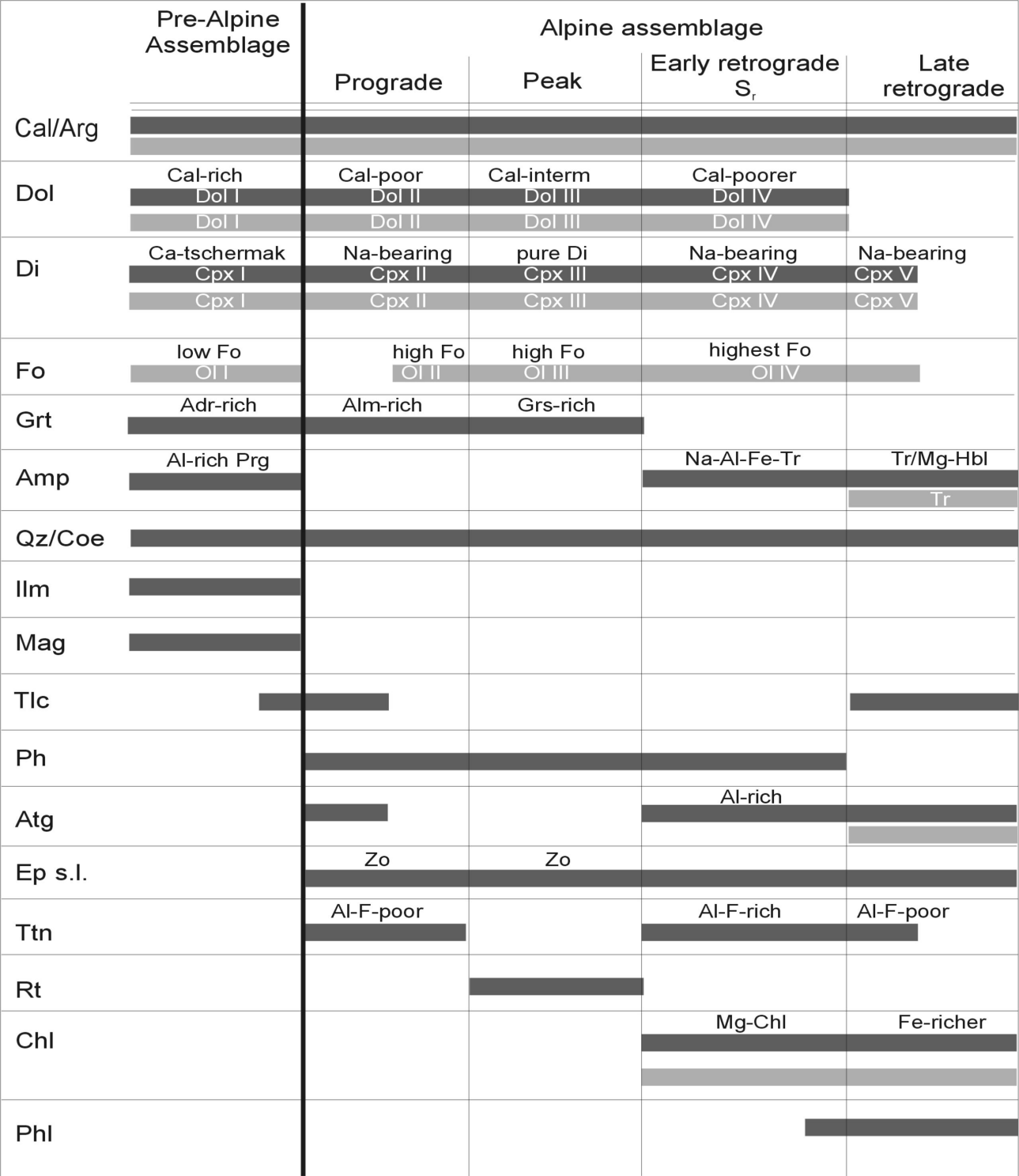


Figure 4

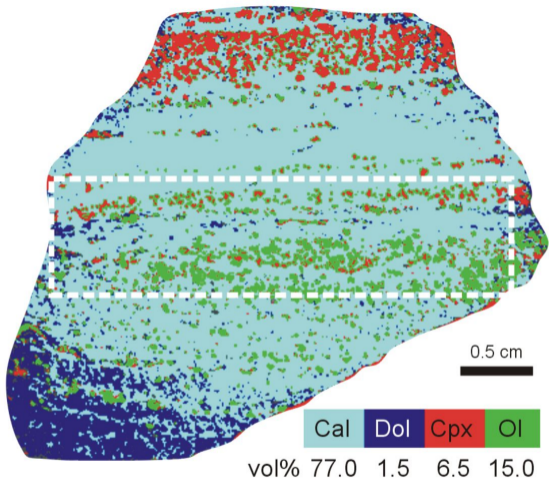


Figure 5

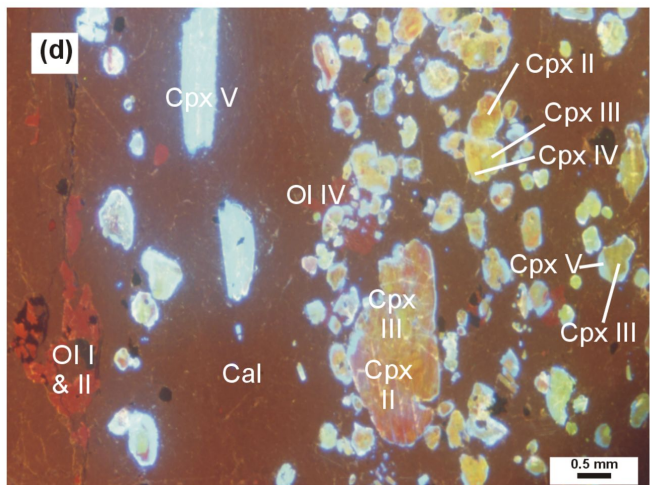
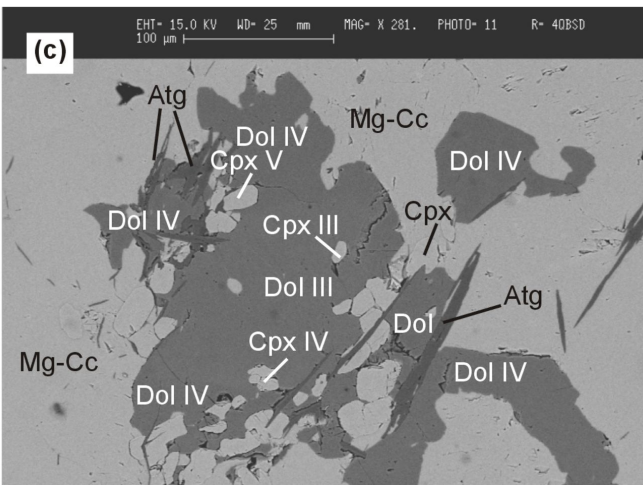
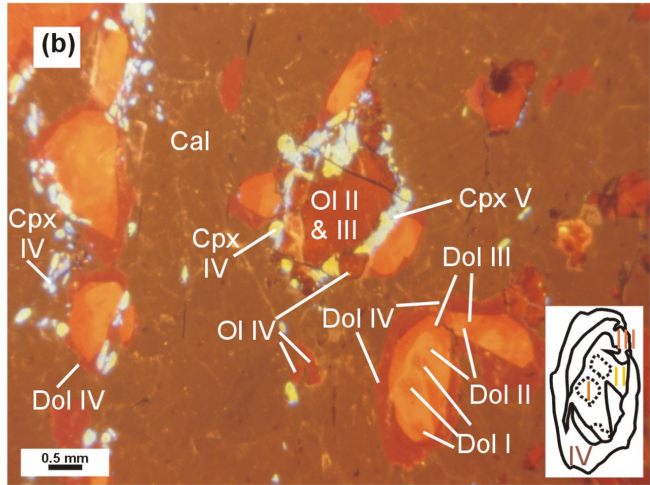
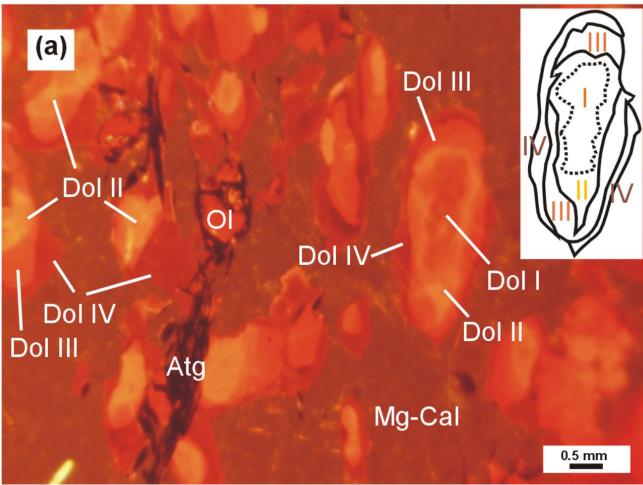


Figure 6

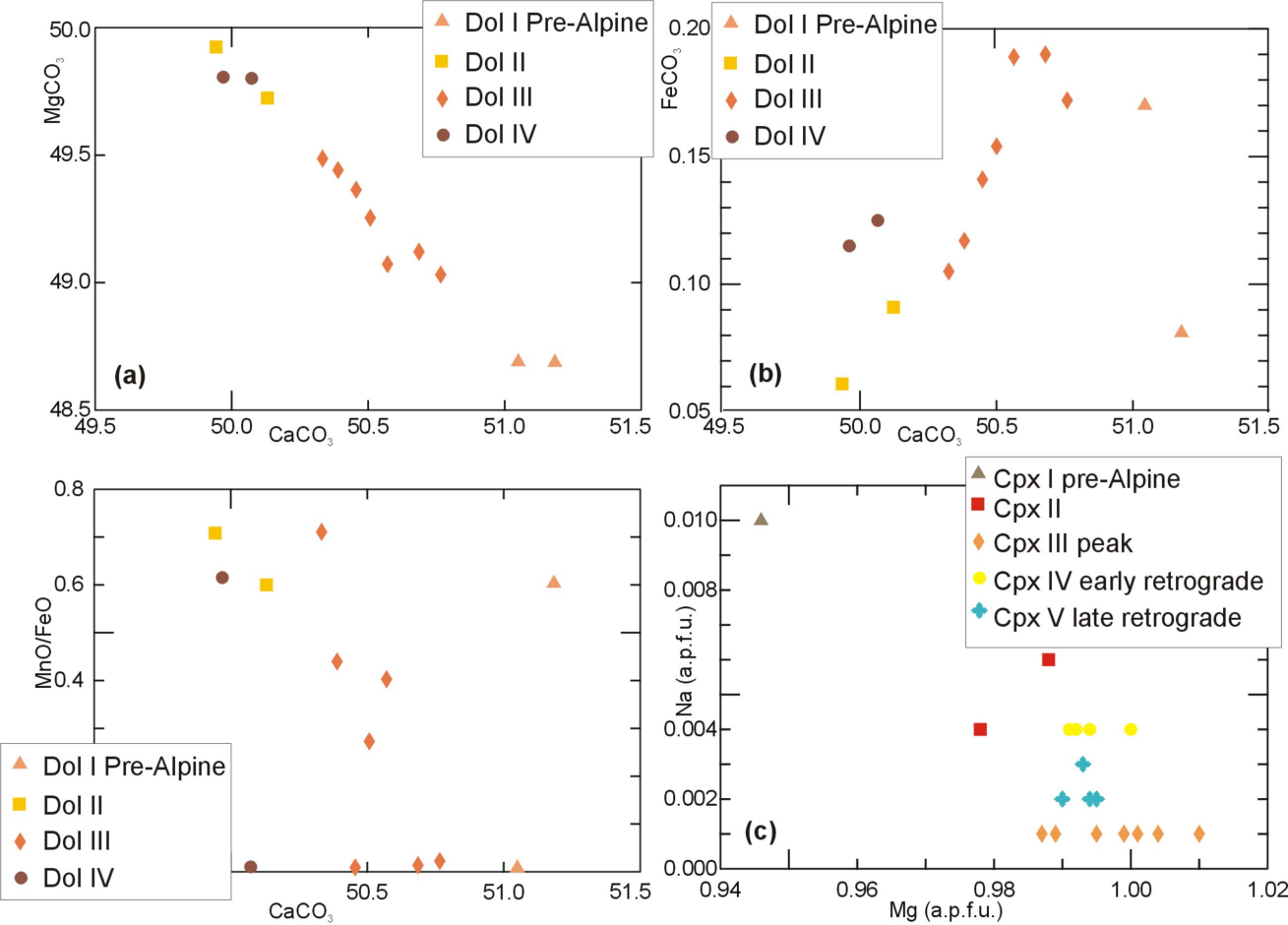


Figure 7

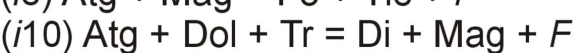
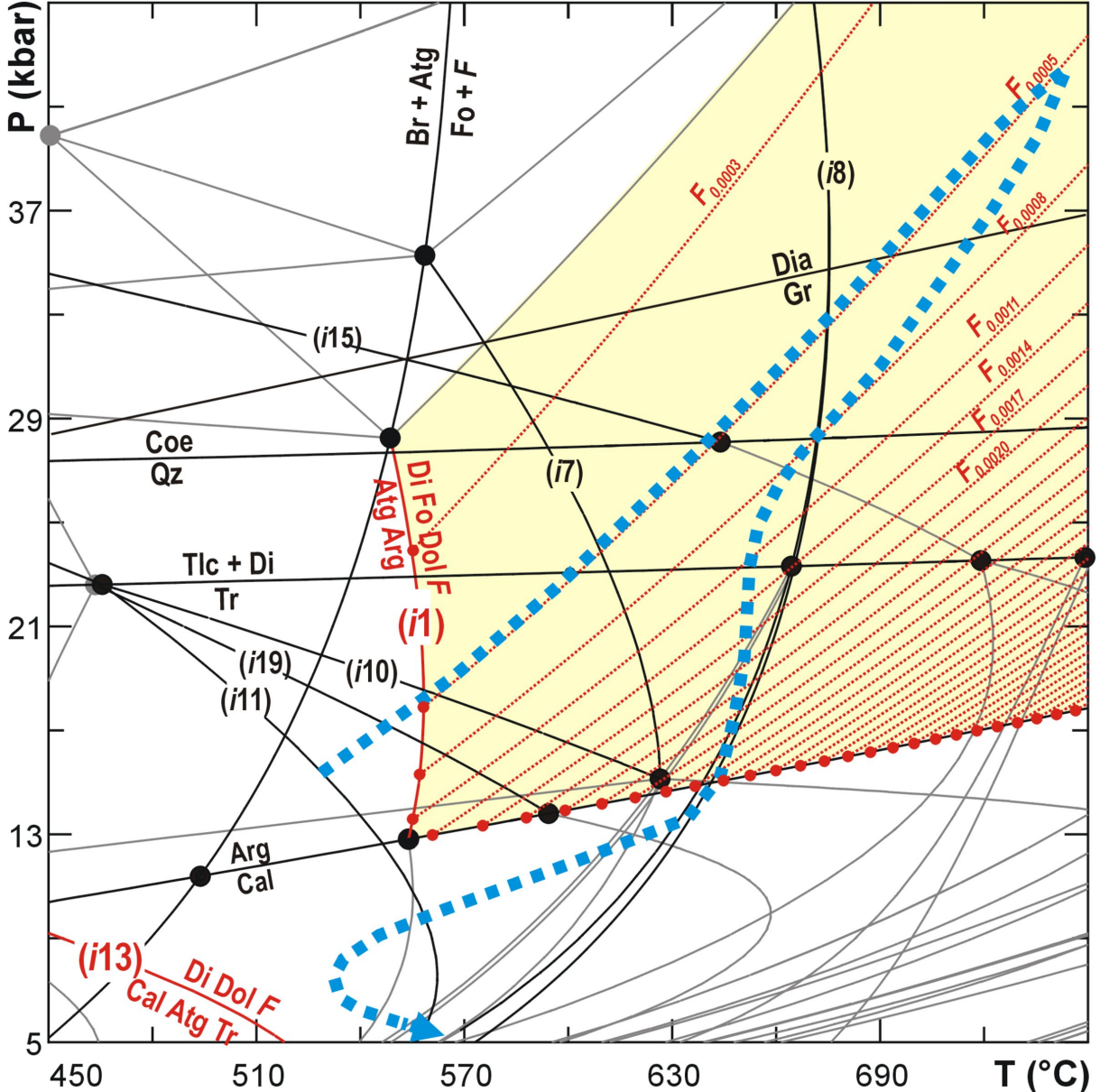


Figure 8

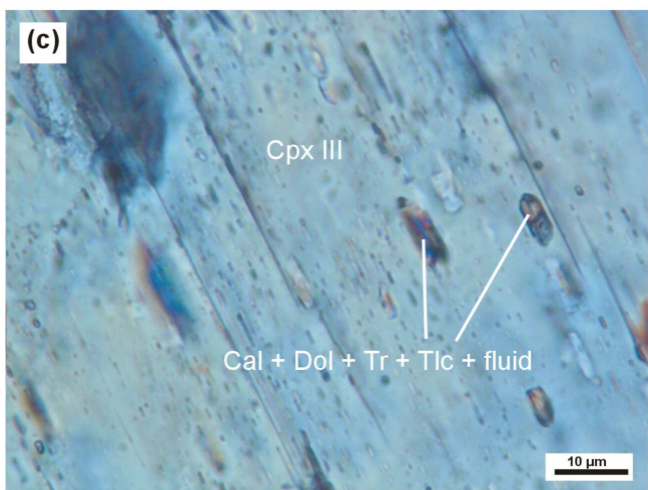
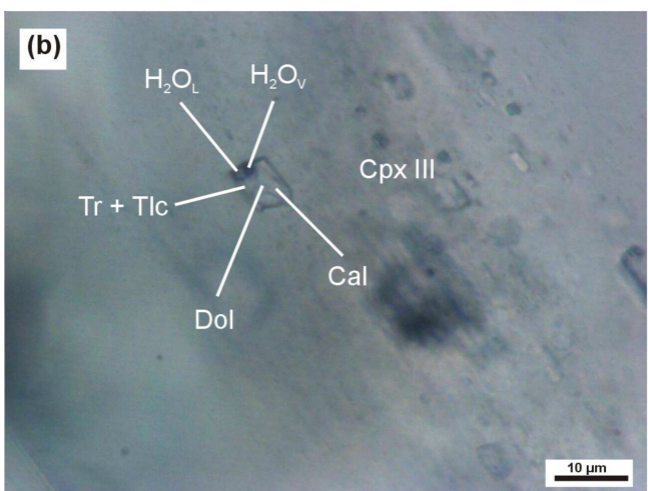
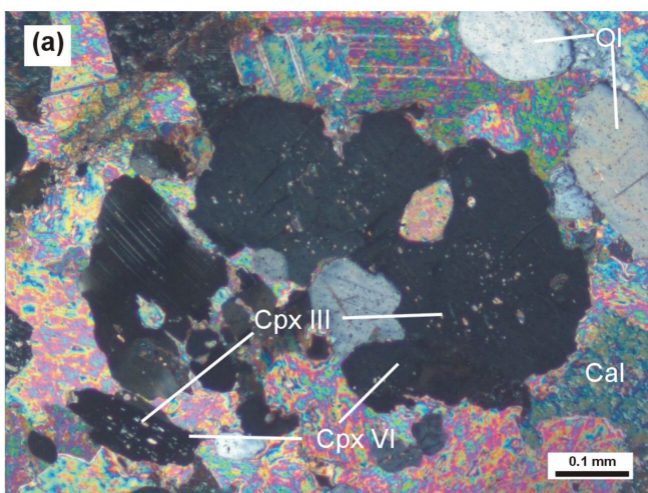


Figure 9

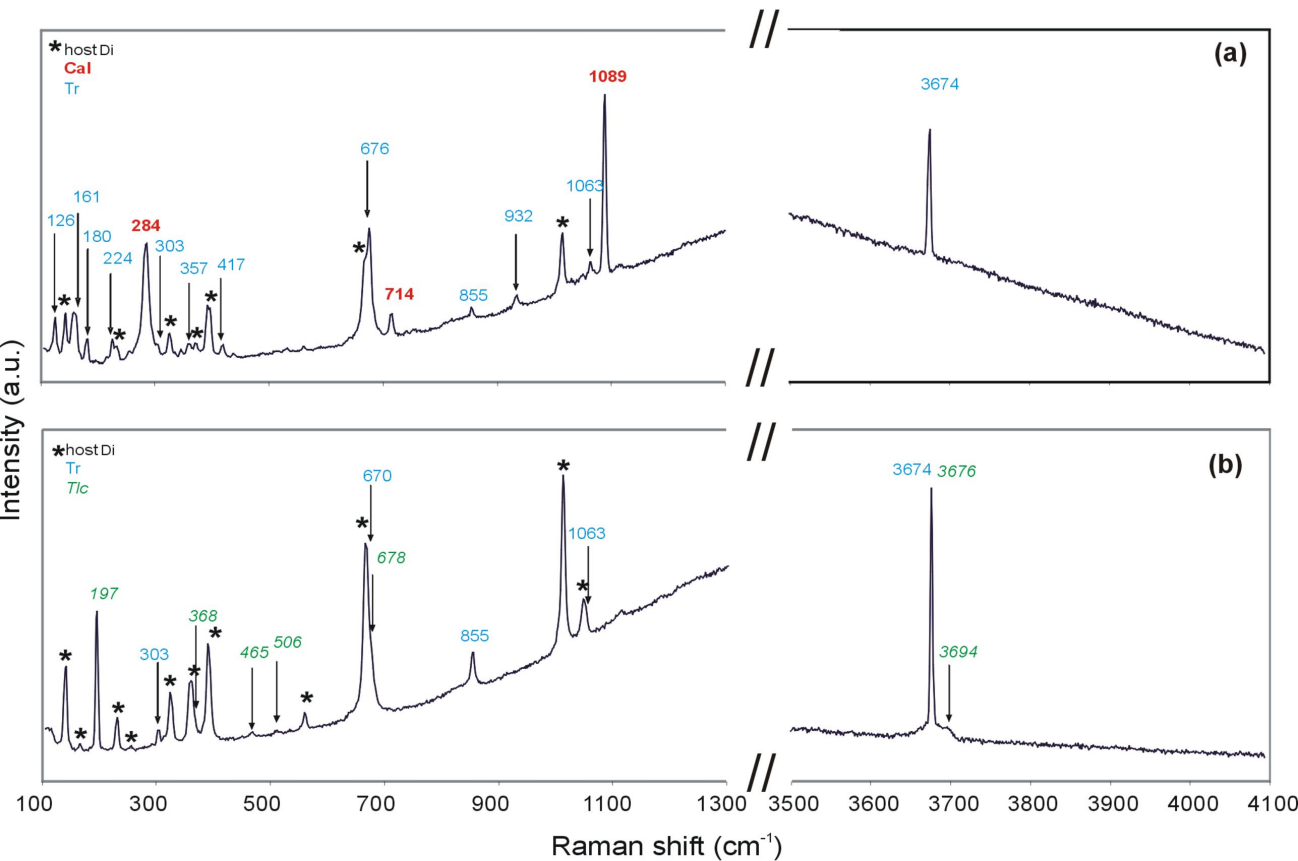


Figure 10

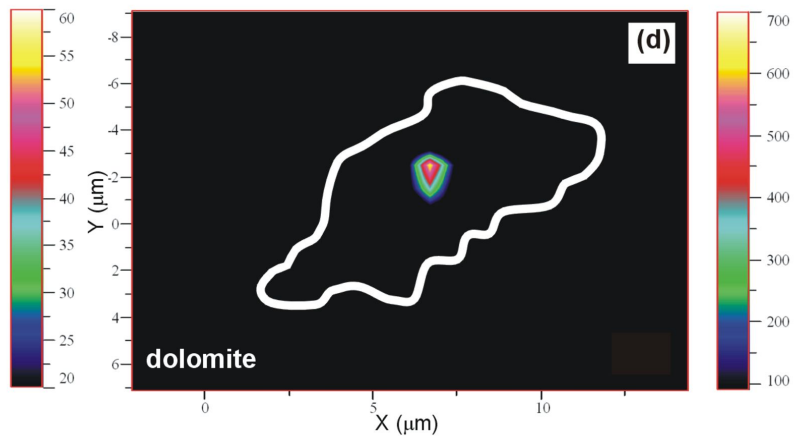
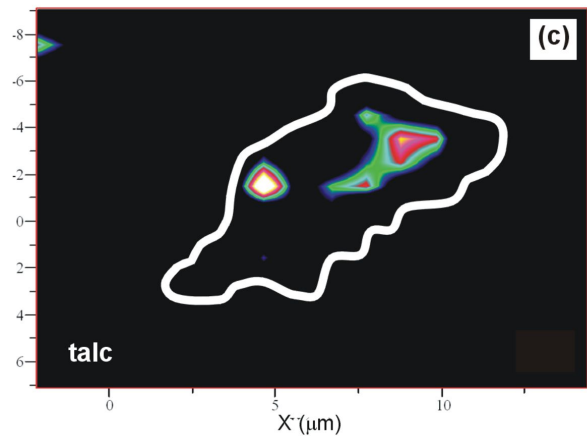
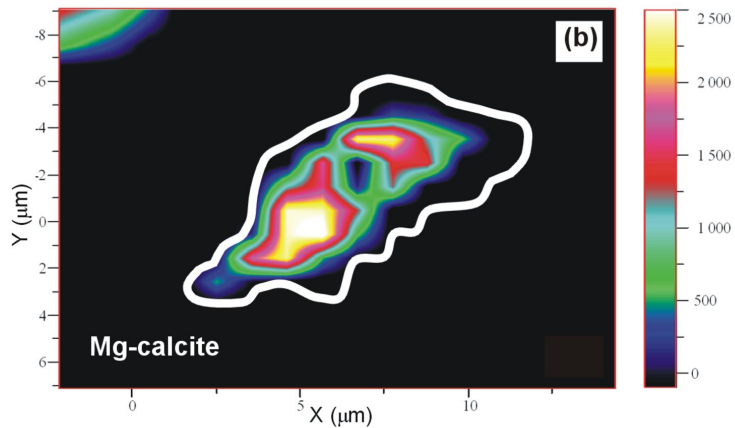
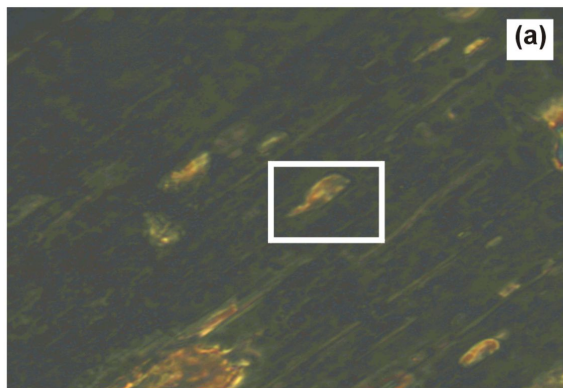


Figure 11

Table 1: list of the studied samples

	Sample	Lithology	Main forming minerals	Locality
C(F)M(A)S-COH system	DM675 (layer)	Atg-Ol-Cpx-rich calcite-dolomite marble	Dol, Cc, Atg, Ol, Cpx, Chl	Costa Monforte
	DM675 (layer)	Ol-Atg-Chl-Amp-rich calcite-dolomite marble	Dol, Cc, Ol, Atg, Chl, Amp	Costa Monforte
	DM675 (layer)	Ol-Cpx-Atg-Chl-Amp-rich calcite-dolomite marble	Dol, Cc, Ol, Cpx, Atg, Chl, Amp	Costa Monforte
	DM1170 (layer)	Chl-rich calcite-dolomite marble	Dol, Cc, Chl, Rt	Costa Monforte
	DM1170 (layer)	Atg-Chl-rich calcite-dolomite marble	Dol, Cc, Atg, Chl, Amp	Costa Monforte
	DM1638 (layer)	Chl-Cpx-rich calcite-dolomite marble	Dol, Cc, Chl, Cpx, Amp	Isasca
	DM1638 (layer)	Atg-Chl-rich calcite-dolomite marble	Dol, Cc, Atg, Chl, Amp	Isasca
(N)CFM(A)S-COH system	DM1631	Cpx-Amp-rich calcite-dolomite marble	Dol, Cc, Cpx, Amp	Costa Monforte
	DM1649 (layer)	Cpx-Chl-rich calcite-dolomite marble	Dol, Cc, Cpx, Chl, Amp	Isasca
	DM1657 (layer)	Amp-Chl-rich calcite-dolomite marble	Dol, Cc, Amp, Chl	Costa Monforte
NKCFMAS-COH system	DM1636	Wm-Amp-Chl-rich calcite-dolomite marble		Costa Monforte
	DM1649 (layer)	Wm-rich calcite-dolomite marble	Dol, Cc, Wm	Isasca
	DM1649 (layer)	Cpx-Zo-Wm-Ttn-rich calcite-dolomite marble	Dol, Cc, Cpx, Zo, Wm, Amp, Ttn	Isasca
	DM1649 (layer)	Cpx-Wm-Qz-rich calcite-dolomite marble	Dol, Cc, Cpx, Wm, Qz, Amp, Ep, Ttn	Isasca
	DM1657 (layer)	Wm-Amp-Chl-Cpx-rich calcite-dolomite marble	Dol, Cc, Wm, Amp, Chl, Cpx	Costa Monforte
	ADM17	Wm-Amp-Chl-Grt-Cpx-rich calcite-dolomite marble	Dol, Cc, Wm, Amp, Chl, Grt, Cpx, Qz, Chl, Ep	Costa Monforte

Table 2: representative chemical composition of silicates from the impure calcite-dolomite marbles

Sample	DM1636	DM1636	DM675	DM675	DM1636	DM675	DM675	DM675	DM675
Metam. stage	pre-Alpine	pre-Alpine	pre-Alpine	pre-Alpine	prograde	prograde	prograde	prograde	prograde
Location	Dol inner c	Dol inner c			Dol outer c				
Mineral	Grt	Cpx I	Cpx I	OI I	Grt	Cpx II	Cpx II	OI II	OI II
No.	grtN11a	cpxN15b	29-28	29-20	grtN7b	25-3	22b-40	25-1	25-36
Anal. technique	EDS-WDS*	EDS-WDS*	WDS	WDS	EDS-WDS*	WDS	WDS	WDS	WDS
SiO ₂	39.22	53.83	55.63	42.60	40.93	55.04	55.86	42.35	41.69
TiO ₂	1.04	0.24	b.d.l.	b.d.l.	0.15	b.d.l.	b.d.l.	0.00	0.00
Cr ₂ O ₃	b.d.l.	b.d.l.	b.d.l.	0.06	b.d.l.	b.d.l.	b.d.l.	0.01	0.06
Al ₂ O ₃	21.90	2.06	0.41	b.d.l.	23.31	0.14	0.14	0.00	0.01
Fe ₂ O ₃ *						0.71			
FeO	3.16	0.62	1.38	1.37	3.79		0.35	0.62	0.64
MnO	0.23	b.d.l.	0.07	0.10	0.21	0.03	0.01	0.01	0.02
MgO	3.28	18.53	17.67	56.68	6.91	18.23	18.51	57.86	57.66
NiO	-	-	0.09	0.03	-	b.d.l.	b.d.l.	b.d.l.	b.d.l.
CaO	30.36	24.93	25.49	0.10	25.17	26.17	25.76	0.01	b.d.l.
Na ₂ O	b.d.l.	0.09	0.15	b.d.l.	b.d.l.	0.05	0.08	0.01	0.01
K ₂ O	b.d.l.	b.d.l.	b.d.l.	b.d.l.	b.d.l.	0.01	b.d.l.	0.01	b.d.l.
F	b.d.l.	b.d.l.	b.d.l.	-	b.d.l.	b.d.l.	b.d.l.	-	-
Total	99.19	100.29	100.89	100.94	100.47	100.38	100.71	100.88	100.09
Si	2.96	1.93	1.999	0.995	3.00	1.982	2.001	0.984	0.975
Ti	0.06	0.01			0.01			0.000	0.000
Cr				0.001				0.000	0.001
Al	1.95	0.09	0.017		2.01	0.006	0.006	0.000	0.000
Fe ³⁺	0.02	0.02			0.00	0.019	0.000	0.000	0.000
Fe ²⁺	0.18	0.00	0.042	0.027	0.23	0.000	0.011	0.012	0.013
Mn	0.02		0.002	0.002	0.01	0.001	0.000	0.000	
Mg	0.37	0.99	0.946	1.973	0.75	0.978	0.988	2.003	2.010
Ni	-	-	0.003	0.001	-				
Ca	2.45	0.96	0.981	0.003	1.97	1.010	0.989	0.000	0.000
Na		0.006	0.010			0.004	0.006	0.001	0.001
K						0.001		0.000	
F								-	-
Mg#				0.983				0.994	0.994

Notes: EDS-WDS* = WDS data for Na and F; Fe₂O₃* = calculated; "-" = not measured; b.d.l. = below detection limit; Mg# = Mg/(Mg+Fe²⁺);

Table 2: representative chemical composition of silicates from the impure calcite-dolomite marbles (continue)

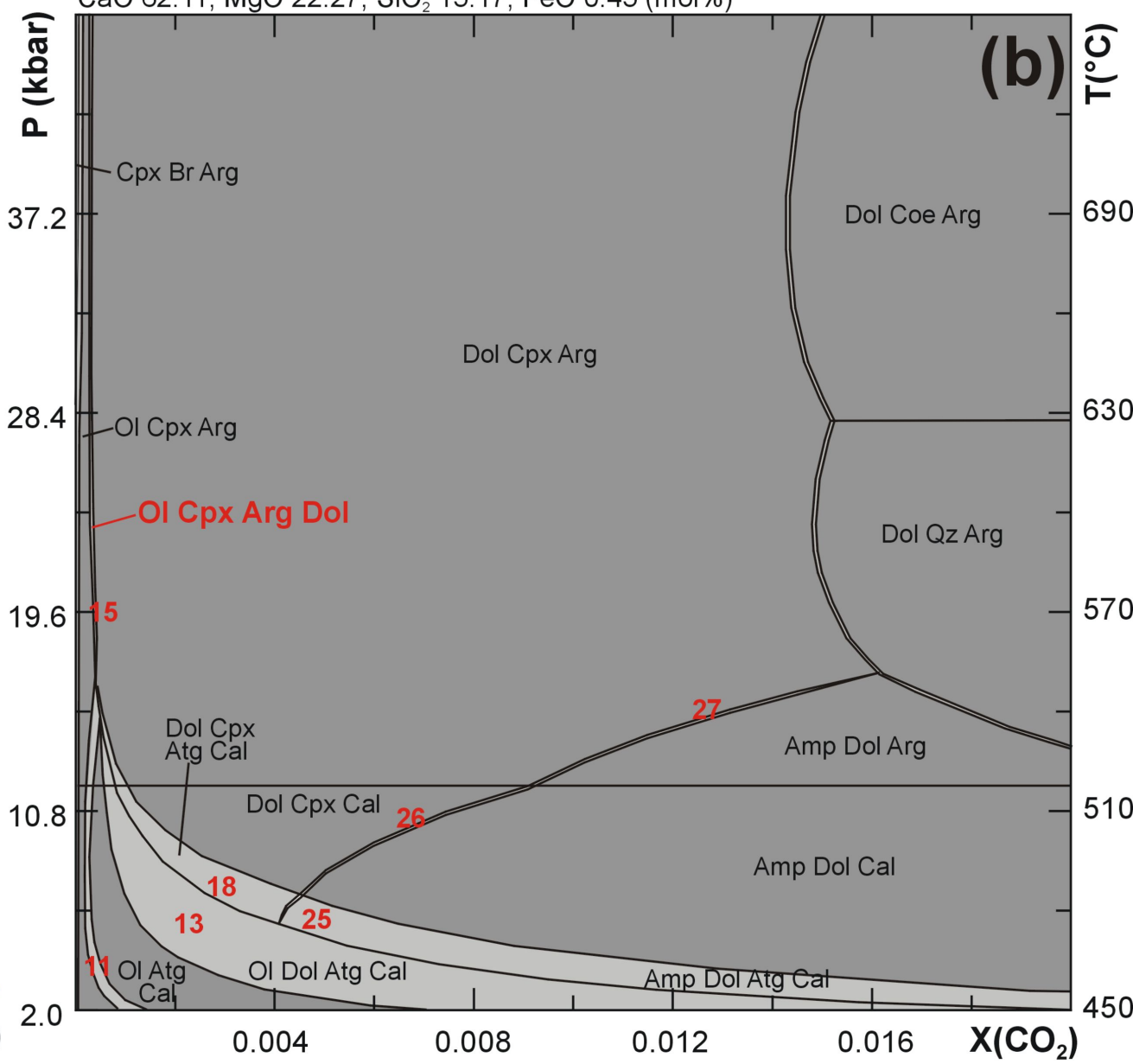
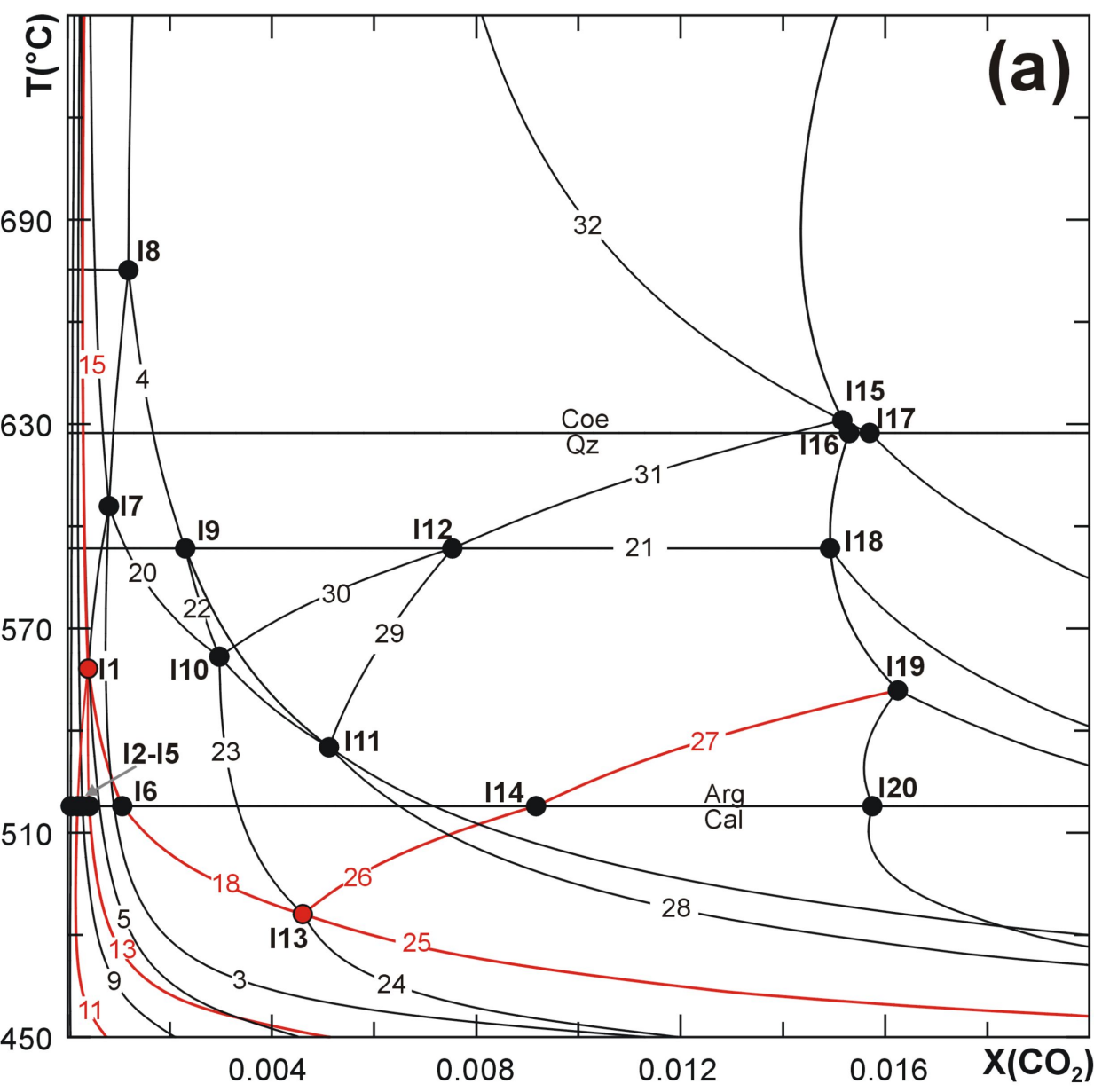
Sample	DM1636	DM1636	DM675	DM675	DM675	DM675	DM675	DM675	ADM17	DM675	DM675	DM675
Metam. stage	peak	peak	peak	peak	peak	peak	early retrograde	early retrograde	early retrograde	early retrograde	late retrograde	late retrograde
Location	Dol inner r	Dol inner r							Dol outer r			
Mineral	Grt	Phg	Cpx III	Cpx III	OI III	OI III	Cpx IV	Cpx IV	Phl	OI IV	Cpx V	Cpx V
No.	grtN1b	Nphe2	25-5	22b-38	25-2	25-37	22-10	22x-24	67phl1_in_dol	18-34	29-30	22b-39
Anal. technique	EDS-WDS*	EDS-WDS*	WDS	WDS	WDS	WDS	WDS	WDS	EDS-WDS*	WDS	WDS	WDS
SiO ₂	40.29	53.58	55.77	55.87	42.21	42.53	55.93	55.58	41.14	42.54	55.70	56.20
TiO ₂	0.25	0.49	b.d.l.	0.03	0.02	0.04	b.d.l.	b.d.l.	b.d.l.	b.d.l.	0.01	0.03
Cr ₂ O ₃	b.d.l.	b.d.l.	0.04	b.d.l.	0.09	0.03	b.d.l.	b.d.l.	b.d.l.	b.d.l.	b.d.l.	b.d.l.
Al ₂ O ₃	22.64	23.38	0.02	0.01	b.d.l.	b.d.l.	b.d.l.	0.02	13.34	b.d.l.	0.06	0.04
Fe ₂ O ₃ *							0.02				0.08	
FeO	3.44	0.26	0.12	0.16	0.56	0.55	0.18	0.27	3.79	0.45	b.d.l.	0.14
MnO	0.33	b.d.l.	0.01	0.01	0.03	b.d.l.	b.d.l.	0.02	b.d.l.	b.d.l.	0.02	0.03
MgO	6.20	6.65	18.47	18.70	57.38	58.04	18.57	18.57	25.85	58.10	18.64	18.63
NiO	-	-	b.d.l.	b.d.l.	0.01	0.07	0.07	0.00	-	0.01	0.03	b.d.l.
CaO	25.97	b.d.l.	26.05	25.85	0.05	0.04	25.97	25.25	0.24	0.04	26.13	25.73
Na ₂ O	b.d.l.	0.06	b.d.l.	b.d.l.	0.01	b.d.l.	0.05	0.06	0.04	b.d.l.	0.03	0.04
K ₂ O	b.d.l.	11.64	0.01	b.d.l.	b.d.l.	b.d.l.	0.01	0.04	10.89	0.03	b.d.l.	b.d.l.
F	b.d.l.	b.d.l.	b.d.l.	b.d.l.	-	-	b.d.l.	b.d.l.	0.86	-	b.d.l.	b.d.l.
Total	99.12	96.05	100.49	100.63	100.36	101.30	100.80	99.81	96.15	101.17	100.70	100.84
Si	3.00	3.53	2.003	2.002	0.986	0.984	2.002	2.008	2.92	0.985	1.994	2.010
Ti	0.01	0.02		0.001	0.000	0.001					0.000	0.001
Cr			0.001		0.002	0.001						
Al	1.99	1.82	0.001	0.000				0.001	1.12		0.003	0.002
Fe ³⁺							0.001				0.002	
Fe ²⁺	0.21	0.01	0.004	0.005	0.011	0.011	0.005	0.008	0.23	0.009		0.004
Mn	0.02	0.00	0.000	0.000	0.001	0.000		0.001			0.001	0.001
Mg	0.69	0.65	0.989	0.999	1.998	2.002	0.991	1.000	2.74	2.005	0.995	0.993
Ni	-	-			0.000	0.001	0.002	0.000	-	0.000	0.001	
Ca	2.07		1.002	0.993	0.001	0.001	0.996	0.977	0.02	0.001	1.002	0.986
Na		0.007			0.001	0.000	0.004	0.004	0.005		0.002	0.003
K		0.98	0.001				0.001	0.002	0.99	0.001		
F					-	-			0.192	-		
Mg#					0.993	0.993			0.92	0.995		

Notes: EDS-WDS* = WDS data for Na and F; Fe₂O₃* = calculated; "-" = not measured; b.d.l. = below detection limit; Mg# = Mg/(Mg+Fe²⁺);

Table 3: representative chemical composition of dolomite from sample DM675

Sample	DM675	DM675	DM675	DM675	DM675	DM675	DM675	DM675	DM675	DM675	DM675	DM675	DM675
Metam. stage	pre-Alpine	pre-Alpine	prograde	prograde	peak	peak	peak	peak	peak	peak	peak	early retrograde	early retrograde
Location	Dol inner c	Dol inner c	Dol outer c	Dol outer c	Dol inner r	Dol inner r	Dol inner r	Dol inner r	Dol inner r	Dol inner r	Dol inner r	Dol outer r	Dol outer r
No.	DM675-18-17	DM675-18-18	DM675-18-16	DM675-29-31	DM675-25-7	DM675-18-15	DM675-25-8	DM675-18-14	DM675-29-23	DM675-29-32	DM675-18-35	DM675-25-6	DM675-29-33
Anal. technique	WDS	WDS	WDS	WDS	WDS	WDS	WDS	WDS	WDS	WDS	WDS	WDS	WDS
SiO ₂	0.039	0.001	0.008	0.025	b.d.l.	b.d.l.	0.009	b.d.l.	0.025	0.029	0.003	0.012	b.d.l.
TiO ₂	b.d.l.	0.002	b.d.l.	0.025	b.d.l.	b.d.l.	0.008	b.d.l.	0.041	b.d.l.	0.025	0.002	0.029
NiO	b.d.l.	0.065	0.080	b.d.l.	b.d.l.	b.d.l.	b.d.l.	0.052	b.d.l.	0.079	0.077	0.161	0.149
Cr ₂ O ₃	0.016	0.036	0.077	b.d.l.	0.082	0.037	0.046	b.d.l.	b.d.l.	0.176	0.014	0.018	0.034
Al ₂ O ₃	0.009	0.056	0.025	b.d.l.	0.015	0.000	b.d.l.	b.d.l.	0.038	b.d.l.	0.025	b.d.l.	0.058
FeO	0.183	0.212	0.048	0.070	0.135	0.083	0.121	0.091	0.146	0.149	0.111	0.091	0.098
MnO	0.033	0.097	0.034	0.042	0.003	0.059	0.033	0.040	0.002	0.060	0.001	0.056	0.001
MgO	21.671	21.422	21.837	21.638	21.555	21.804	21.754	21.621	21.190	21.754	21.688	22.185	21.887
CaO	29.802	30.250	30.390	30.348	31.048	30.852	31.034	30.656	30.418	31.188	30.838	30.964	30.614
Na ₂ O	0.023	b.d.l.	b.d.l.	0.044	b.d.l.	b.d.l.	0.037	0.005	b.d.l.	0.061	b.d.l.	0.029	0.038
K ₂ O	0.032	b.d.l.	0.031	0.007	b.d.l.	0.023	0.014	0.018	b.d.l.	0.004	0.031	0.031	0.008
SrO	0.102	b.d.l.	b.d.l.	b.d.l.	b.d.l.	b.d.l.	b.d.l.	b.d.l.	b.d.l.	0.103	0.044	0.044	b.d.l.
BaO	b.d.l.	b.d.l.	0.046	b.d.l.	0.044	b.d.l.	0.070	b.d.l.	b.d.l.	b.d.l.	b.d.l.	b.d.l.	b.d.l.
ZrO ₂	0.043	0.103	0.061	b.d.l.	b.d.l.	0.005	0.020	b.d.l.	b.d.l.	b.d.l.	b.d.l.	b.d.l.	0.076
P ₂ O ₅	b.d.l.	b.d.l.	b.d.l.	b.d.l.	0.077	b.d.l.	b.d.l.	0.044	0.077	b.d.l.	0.045	0.088	0.022
Cl	0.008	0.007	b.d.l.	0.009	b.d.l.	b.d.l.	0.014	0.004	b.d.l.	b.d.l.	b.d.l.	0.024	0.007
CO ₂	47.602	48.186	47.876	47.577	48.049	48.125	48.284	47.800	47.180	48.565	48.069	48.802	48.183
Tot	100.105	101.351	100.514	99.785	101.007	100.986	101.443	100.333	99.118	102.169	100.969	102.508	101.204
O=Cl	2.184	2.042	0.000	2.666	0.000	0.000	3.886	1.248	0.000	0.000	0.000	6.835	1.900
Total	97.921	99.309	100.514	97.119	101.007	100.986	97.558	99.085	99.118	102.169	100.969	95.673	99.304
CaCO ₃	51.05	51.18	49.94	50.13	50.77	50.33	50.51	50.39	50.69	50.57	50.46	49.97	50.07
MgCO ₃	48.69	48.69	49.92	49.72	49.03	49.49	49.25	49.44	49.12	49.07	49.36	49.81	49.80
MnCO ₃	0.00	0.05	0.04	0.05	0.00	0.08	0.04	0.05	0.00	0.08	0.00	0.07	0.00
FeCO ₃	0.17	0.08	0.06	0.09	0.17	0.11	0.15	0.12	0.19	0.19	0.14	0.11	0.13
SrCO ₃	0.09	0.00	0.00	0.00	0.00	0.00	0.00	0.00	0.00	0.09	0.04	0.04	0.00
BaCO ₃	0.00	0.00	0.03	0.00	0.03	0.00	0.04	0.00	0.00	0.00	0.00	0.00	0.00

Notes: b.d.l. = below detection limit



- | | | | | | | |
|------------------|-------------------|----------------------|----------------------|----------------------|----------------------|----------------------|
| 1: Atg = Tlc Fo | 6: Br Di = Fo Cal | 11: Fo Di = Cal Atg | 16: Atg Dol = Fo Di | 21: Tr = Tlc Di | 26: Cal Tr = Di Dol | 31: Dol Tlc = Di Mag |
| 2: Tlc Mag = Fo | 7: Br Di = Fo Arg | 12: Arg Atg = Fo Di | 17: Arg Atg = Di Dol | 22: Di Atg = Mag Tr | 27: Arg Tr = Di Dol | 32: Mag Coe = Tlc |
| 3: Atg Mag = Fo | 8: Cal = Arg | 13: Fo Cal = Dol Atg | 18: Cal Atg = Di Dol | 23: Di Atg = Dol Tr | 28: Atg Tr = Dol Tlc | |
| 4: Atg = Tlc Mag | 9: Br Cal = Dol | 14: Fo Arg = Dol Atg | 19: Fo Dol = Di Mag | 24: Di Atg = Cal Tr | 29: Dol Tlc = Mag Tr | |
| 5: Br = Mag | 10: Br Arg = Dol | 15: Fo Arg = Di Dol | 20: Atg Dol = Di Mag | 25: Cal Atg = Dol Tr | 30: Dol Tr = Di Mag | |

Figure S1

Table supp mat 1: chemical composition of silicates from the impure calcite-dolomite marbles

Sample	DM675	DM675	DM675	DM675	DM675	DM675	DM675	DM675	ADM17
Metam. stage	peak	peak	peak	peak	peak	peak	early retrograde	early retrograde	early retrograde
Mineral	Cpx III	Cpx III	Cpx III	Cpx III	Cpx III	Cpx III	Cpx IV	Cpx IV	Al-rich Ttn
No.	22-9	22b-12	22b-13	22x-25	22x-26	22x-27	22-11	22b-42	tit1
Anal. technique	WDS	WDS	WDS	WDS	WDS	WDS	WDS	WDS	EDS-WDS*
SiO2	55.77	55.17	55.74	55.41	55.77	55.77	55.65	55.28	30.79
TiO2	b.d.l.	0.02	b.d.l.	b.d.l.	0.06	b.d.l.	b.d.l.	b.d.l.	33.74
Cr2O3	0.04	0.01	b.d.l.	0.05	0.02	b.d.l.	b.d.l.	b.d.l.	b.d.l.
Al2O3	0.02	b.d.l.	b.d.l.	0.06	0.01	b.d.l.	b.d.l.	0.01	4.564
Fe2O3*		0.24	0.16				0.24	0.21	
FeO	0.12	0.00	0.00	0.27	0.23	0.18	0.00	0.08	b.d.l.
MnO	0.01	0.05	0.07	b.d.l.	0.07	0.03	b.d.l.	0.03	b.d.l.
MgO	18.47	18.59	18.79	18.21	18.61	18.86	18.63	18.41	b.d.l.
NiO	b.d.l.	0.06	b.d.l.	b.d.l.	0.02	0.09	b.d.l.	b.d.l.	-
CaO	26.05	25.88	25.83	25.25	25.80	25.36	26.14	25.68	28.12
Na2O	b.d.l.	0.02	b.d.l.	0.02	0.02	0.01	0.06	0.06	b.d.l.
K2O	0.01	b.d.l.	0.01	b.d.l.	b.d.l.	0.02	0.01	b.d.l.	b.d.l.
F	b.d.l.	b.d.l.	b.d.l.	b.d.l.	b.d.l.	b.d.l.	b.d.l.	b.d.l.	1.01
Total	100.49	100.04	100.60	99.27	100.61	100.32	100.73	99.76	98.22
Si	2.003	1.989	1.998	2.015	2.000	2.004	1.992	1.999	1.02
Ti		0.001			0.002				0.84
Cr	0.001	0.000		0.001	0.001				
Al	0.001			0.003	0.000			0.000	0.18
Fe3		0.007	0.004				0.007	0.006	
Fe2	0.004	0.000	0.000	0.008	0.007	0.005	0.000	0.003	
Mn	0.000	0.002	0.002	0.000	0.002	0.001		0.001	
Mg	0.989	0.999	1.004	0.987	0.995	1.010	0.994	0.992	
Ni		0.002			0.001	0.003			-
Ca	1.002	1.000	0.992	0.984	0.991	0.976	1.003	0.995	1.00
Na		0.001		0.001	0.001	0.001	0.004	0.004	
K	0.001		0.001			0.001	0.001		
F									0.106

Notes: EDS-WDS* = WDS data for Na and F; Fe₂O₃* = calculated; "-" = not measured; b.d.l. = below detection limit

Table supp mat 1: chemical composition of silicates from the impure calcite-dolomite marbles (continue)

Sample	DM675	DM675	ADM17	DM1636	ADM17	ADM17	ADM17
Metam. stage	late retrograde	late retrograde	late retrograde	late retrograde	late retrograde	late retrograde	late retrograde
Mineral	Cpx V	Cpx V	Al-poorTtn	Tlc	Mg-Hbl	Tr	Tr
No.	29-29	22b-41	tit2	tlcX	39tre1	3tre2	39tre2
Anal. technique	WDS	WDS	EDS-WDS*	EDS-WDS*	EDS-WDS*	EDS-WDS*	EDS-WDS*
SiO2	55.22	55.80	30.50	62.06	54.46	56.62	56.80
TiO2	0.03	b.d.l.	36.55	b.d.l.	0.294	b.d.l.	b.d.l.
Cr2O3	b.d.l.	0.02	b.d.l.	b.d.l.	b.d.l.	b.d.l.	b.d.l.
Al2O3	0.05	0.03	2.49	b.d.l.	6.234	2.095	1.63
Fe2O3*	0.39						
FeO	0.00	0.18	0.35	1.50	3.32	3.22	3.56
MnO	0.04	b.d.l.	b.d.l.	b.d.l.	b.d.l.	b.d.l.	b.d.l.
MgO	18.50	18.53	b.d.l.	30.65	20.22	22.34	21.76
NiO	0.15	b.d.l.	-	-	-	-	-
CaO	25.75	26.01	27.66	2.03	11.39	12.96	12.18
Na2O	0.03	0.03	b.d.l.	0.08	1.52	0.44	0.55
K2O	b.d.l.	b.d.l.	b.d.l.	b.d.l.	0.19	b.d.l.	0.09
F	b.d.l.	b.d.l.	0.62	0.21	0.239	0.219	0.135
Total	100.16	100.60	98.18	96.53	97.87	97.89	96.71
Si	1.990	2.001	1.01	3.939	7.47	7.76	7.88
Ti	0.001		0.91		0.03		
Cr		0.001					
Al	0.002	0.001	0.10		1.01	0.34	0.27
Fe3	0.011		0.01		0.19	0.16	0.06
Fe2	0.000	0.005	0.00	0.08	0.19	0.21	0.35
Mn	0.001						
Mg	0.994	0.990		2.9	4.13	4.56	4.50
Ni	0.004		-	-	-	-	-
Ca	0.995	0.999	0.99	0.138	1.67	1.90	1.81
Na	0.002	0.002		0.010	0.404	0.117	0.148
K					0.03		0.02
F			0.065	0.042	0.104	0.095	0.059